chemengineering

MDPI

Article

Biogas Cleaning via Vacuum Swing Adsorption Using a Calcium Metal–Organic Framework Adsorbent: A Multiscale Simulation Study

Madison Lasich [1,*], Victoria T. Adeleke [1] and Kaniki Tumba [1,2]

[1] Thermodynamics-Materials-Separations Research Group, Department of Chemical Engineering, Mangosuthu University of Technology, Umlazi 4031, South Africa; adeleke.victoria@mut.ac.za (V.T.A.); tumba@mut.ac.za (K.T.)

[2] School of Mines, Karhale Campus, Université Officielle de Bukavu, Bukavu P.O. Box 570, Democratic Republic of the Congo

* Correspondence: lasich.madison@mut.ac.za

Abstract: Purifying biogas can enhance the performance of distributed smart grid systems while potentially yielding clean feedstock for downstream usage such as steam reforming. Recently, a novel anion-pillared metal–organic framework (MOF) was reported in the literature that shows good capacity to separate acetylene from carbon dioxide. The present study assesses the usefulness of this adsorbent for separating a typical biogas mixture (consisting of methane, nitrogen, oxygen, hydrogen, carbon dioxide, and hydrogen sulphide) using a multiscale approach. This approach couples atomistic Monte Carlo simulations in the grand canonical ensemble with the batch equilibrium modelling of a pressure swing adsorption system. The metal–organic framework displays selectivity at low pressures for carbon dioxide and especially hydrogen sulphide. An analysis of adsorption isotherm models coupled with statistical distributions of surface–gas interaction energies determined that both CH_4 and CO_2 exhibited Langmuir-type adsorption, while H_2S displayed Langmuir-type behaviour at low pressures, with increasing adsorption site heterogeneity at high pressures. Batch equilibrium modelling of a vacuum swing adsorption system to purify a CH_4/CO_2 feedstock demonstrated that such a system can be incorporated into a solar biogas reforming process since the target purity of 93–94 mol-% methane for incorporation into the process was readily achievable.

Keywords: vacuum swing adsorption; multiscale modelling; biogas; metal–organic frameworks; steam reforming

Citation: Lasich, M.; Adeleke, V.T.; Tumba, K. Biogas Cleaning via Vacuum Swing Adsorption Using a Calcium Metal–Organic Framework Adsorbent: A Multiscale Simulation Study. *ChemEngineering* **2024**, *8*, 62. https://doi.org/10.3390/chemengineering8030062

Academic Editor: Yang Yuan

Received: 24 April 2024
Revised: 5 June 2024
Accepted: 7 June 2024
Published: 14 June 2024

1. Introduction

An attractive route for future distributed energy systems as part of a so-called "smart grid" is the adoption of micro-generation or micro-cogeneration systems at the scale of small to medium-sized companies, often within the context of cogeneration whereby a firm may generate both electricity and steam on-site and employ the steam for heating purposes. The use of a biodiesel–biogas fuel compression ignition engine was shown to have superior performance in terms of emissions [1], and such engines can be employed in the generation of electricity or cogeneration processes. The cogeneration of steam and electricity using biogas derived from pig manure and corn silage blends is an area of recent research [2] for which lifecycle aspects such as ozone depletion were examined for a variety of feedstocks, with a view to implement such processes on-site at pig farms. The micro-cogeneration of a compression ignition internal combustion engine using a lean homogeneous air/biogas mixture has been shown to be practicable for a company operating a mid-sized farm [3]. Biomethane fuel obtained from biogas using a solid matrix of wood ash has been shown to be feasible for the purposes of injecting biomethane into the gas grid [4]. The feasibility of biogas as an alternative fuel to generate electricity via a Stirling engine, within the context

of distribution electricity production, has been shown in the literature [5]. Fuel for some of the aforementioned systems could often be in the form of biogas, such as from agricultural wastes, manure, and domestic waste. The composition of biogas is highly variable, as outlined in Table 1, and there are often significant quantities of environmentally harmful compounds such as carbon dioxide and hydrogen sulphide.

Table 1. Typical biogas composition [5].

Component	Volume %
Methane	30–73
Carbon dioxide	20–40
Nitrogen	5–40
Oxygen	0–5
Hydrogen	1–3
Hydrogen sulphide	0–0.1

In addition to the obvious threat to the environment posed by carbon dioxide, hydrogen sulphide is not only toxic, but, in the presence of water, it can cause sulphide stress cracking as it produces corrosive aqueous solutions. Natural gas naturally contains some hydrogen sulphide, with some wells yielding gas with a H_2S content of over 10% [5,6]. Biogas, on the other hand, typically contains up to 0.01% hydrogen sulphide, although it may contain up to 40% carbon dioxide [6], greatly lowering the calorific value of the gas. Moreover, biogas combustion in micro-generation activities will, of course, result in the production of carbon dioxide; hence, removing CO_2 pre-combustion will not only improve the calorific value of the biogas fuel, but will prevent downstream carbon dioxide emissions.

Established biogas upgrading technologies include water scrubbing, physical organic scrubbing, chemical absorption, pressure swing adsorption, membrane separation, and cryogenic separation. These are extensively reviewed in the literature including good illustrations of their respective advantages and disadvantages along with techno-economic analyses examining features such as energy requirements, methane purity, and recovery and cost economics [7–10]. The reader is directed to these thorough review articles for an exhaustive assessment of recent developments in biogas upgrading. Water scrubbing is the simplest and easiest process to operate. However, water contained in biogas often leads to pipe corrosion and clogging due to oxygen presence and bacteria growth, respectively. Furthermore, additional costs arise from the need to dry the final methane-rich stream. While adsorption does not require any heat or harmful chemicals, it exhibits higher methane losses than water scrubbing. The need to address this limitation by developing new adsorbents with improved CO_2 or H_2S-to-methane selectivity motivated the investigation of a metal–organic framework, namely, CaMOF, in the present study.

Metal–organic frameworks (MOFs) represent a class of hybrid organic–inorganic porous materials in which an organic ligand (a nitrogen or oxygen donor) and a metal ion (alkaline metal, transition metal, or a lanthanide) are coordinated to form a tridimensional structure [11,12]. Having emerged nearly three decades ago, MOFs are also referred to as porous coordination polymers, porous coordination networks, microporous coordination polymers, zeolite-like metal–organic frameworks, metal peptide frameworks, metal biomolecule frameworks, or mesoporous metal–organic frameworks [13]. Owing to their advantageous properties such as their porous structure, high specific surface area, good structural stability, high tunability, the existence of active sites, and being readily available, these materials attracted researchers' attention in numerous fields. To date, the known applications of MOFs include drug delivery [14] (Lawson et al., 2021), optoelectronic materials [15], energy storage devices [16], catalysis [17], carbon capture and carbon dioxide conversion to valuable chemicals [18], wastewater treatment [19], and the separation of liquid [20] as well as gas mixtures [21]. In relation to gas separation using MOFs, both membrane and adsorptive processes have been investigated [13]. Selective adsorption, more especially for the separation of light gases, stands out as one of the most attractive

areas of research related to MOFs. This is due to the fact that these gases (oxygen, nitrogen, carbon dioxide, methane) are relevant to environmental pollution remediation scenarios as well as renewable energy systems. These two research themes draw much attention from researchers and the public in the context of worldwide environmental concerns. Examples of extensively investigated systems include CO_2/CH_4 and CO_2/N_2 [22], CO_2/H_2 [23], C_2H_4/C_2H_6 [24], C_3H_6/C_3H_8 [25], and n-C_4H_{10}/i-C_4H_{10} [26]. Li and co-workers (2012) [13] and Lin and co-workers (2020) [27] provided further detail on numerous other separation problems examined in the literature. From both experimental and modelling studies, it emerged that structure and pore properties were identified through these studies as the predominant factors determining separation performance, including the selectivity of MOFs. Furthermore, MOFs were generally found to perform better than zeolites. This stems from challenges in the control of pore structure in zeolites [27].

Previous work has examined the upgrading of biogas using activated carbon [28] and metal–organic frameworks (MOFs) [29] via pressure swing adsorption to enhance the calorific value. With regard to MOFs in particular, core–shell type ionic liquid/MOF composites have been shown to possess exceptionally high selectivity for carbon dioxide over methane [30], while Mg-MOF-74 can be used at low pressure and is widely employed for carbon dioxide adsorption [31]. MOF/polymer membrane composites have been shown to be effective for biogas separation [32–35].

This study's primary focus is on removing undesirable components from biogas using a recently developed Ca^{2+} metal–organic framework (CaMOF) with a honeycomb framework structure [30], as shown in Figure 1 (the crystallographic information file is available in the Supplementary Materials). This MOF possesses high-density organic hydrogen-bonding acceptors and open-metal sites and is already known to be highly effective for separating acetylene from carbon dioxide; hence, it was selected for this exploratory investigation into its potential application as an adsorbent for cleaning biogas. Biogas cleaned of undesirable components can be beneficial in several ways. Firstly, with non-calorific species such as carbon dioxide and nitrogen removed, the heating value of biogas as a fuel can be increased. Secondly, the removal of so-called "sour" components (i.e., carbon dioxide and hydrogen sulphide) can improve the utility of biogas as a feedstock for steam reforming processes to produce synthesis gas and downstream chemicals using renewable biogas as a feedstock. A potential problem with respect to H_2S removal, however, is its tendency to form corrosive solutions in the presence of moisture. This can, of course, limit the lifespan of materials, and so would remain a challenge in terms of the long-term operation of gas sweetening systems that employ the CaMOF or other MOFs.

The MOF in question has a unit cell with parameters a = 3.18746 nm, b = 3.18746 nm, c = 0.89890 nm, $\alpha = \beta = 90.0^\circ$, and $\gamma = 120^\circ$ and the chemical formula $C_{162}H_{180}N_{90}O_{54}Ca_{18}$. Coordinatively unsaturated metal sites, known as open-metal sites, are a common feature of MOF materials and are a key characteristic in terms of enhanced [31–35] and selective [36–39] gas adsorption at low pressures or fugacities. These sites may be unsaturated and made accessible via framework defects such as missing organic linkers [40–42] or, commonly, through chemical [43,44] or thermal [45–49] activation protocols. The CaMOF considered in this study has a honeycomb porous framework with regular 1D channels. The Ca^{2+} cations have a pentagonal bipyramid coordinated geometry and are connected to one oxygen atom in DMA, three nitrogen atoms in the dtztp ligand, and three carboxylate oxygen atoms in the dtztp ligand. The aforementioned channels are lined with exposed Ca^{2+} centres along with uncoordinated nitrogen atoms such that the effective window diameter is 1.5 nm and there is an accessible voidage of 68.9% [30].

The aim of this study is to assess the feasibility of the newly developed CaMOF to separate undesirable sour components from biogas, specifically CO_2 and H_2S. Multicomponent molecular simulations of biogas blended with this adsorbent have not been published in the open literature. The batch equilibrium modelling of a pressure swing adsorption system using this adsorbent, another topic of analysis in this study, has also not been published in the open literature. This study also presents the first investigation into the

incorporation of such a pressure swing adsorption system using the CaMOF into a biogas reforming process.

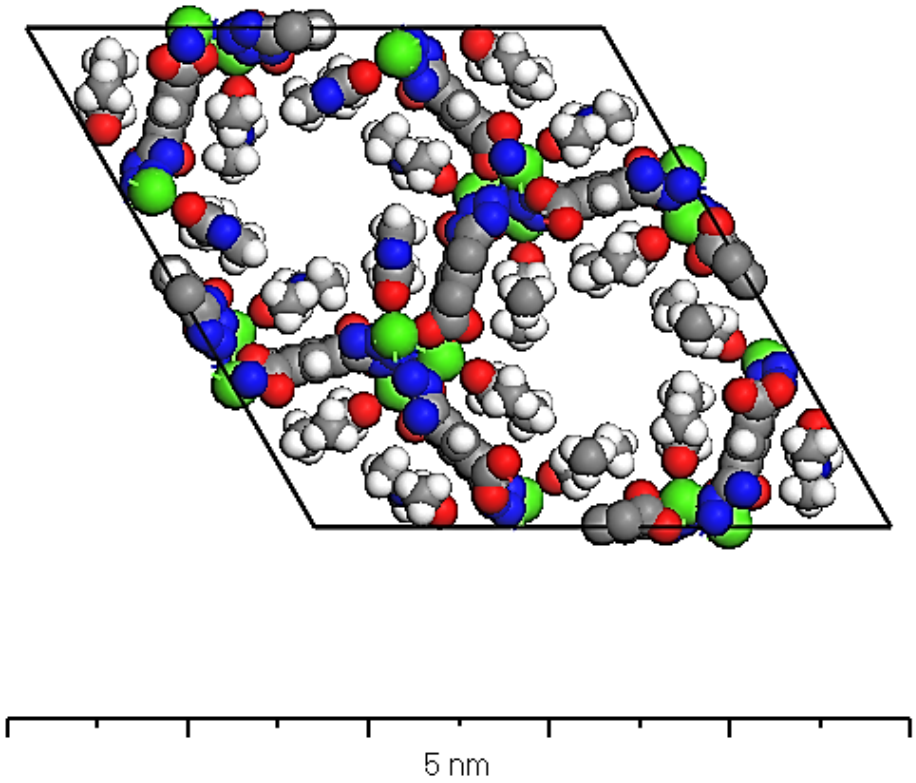

Figure 1. Unit cell of the CaMOF used in this study. Atoms are colour-coded according to the element: white = hydrogen, grey = carbon, red = oxygen, blue = nitrogen, and green = calcium.

2. Methods

To mimic adsorption, Monte Carlo simulations following the Metropolis scheme [50] were employed in the grand canonical ensemble wherein the chemical potential of the fluid reservoir, adsorption cell volume, and system temperature (i.e., T = ambient temperature = 298 K) are fixed. The adsorbent atoms are fixed within the simulation cell while the configuration of adsorbate molecules changes by the application of random moves that mimic real-world behaviour (with their probabilities of occurrence in parentheses): creation (23%), deletion (23%), rotation (24%), translation (24%), and regrowth (6%). The first two moves mimic adsorption and desorption, respectively, while the other three moves mimic the thermal motion of the adsorbed molecules within the simulation cell. Conversion between the chemical potential and the pressure of the gas was undertaken using the Peng–Robinson cubic equation of state [51], which is widely used in natural gas processing and is one of the leading two-constant cubic equations of state [52]. The details of the Metropolis scheme approach to constructing Markov chains from which equilibrium properties can be determined are described in detail in the literature [53]. To ensure equilibration of the system, no less than 2×10^6 moves were used to equilibrate, followed by a further 2×10^7 moves to generate results. Averaging across three independent simulations was undertaken for each data point in the adsorption isotherms, with the standard deviation being used for the estimated uncertainty. Molecular simulations were performed using Dassault Systèmes BIOVIA software 2020: in particular, BIOVIA Materials Studio 2020 [54] was used in this study.

The fully atomistic Condensed-phase Optimized Molecular Potentials for Atomistic Simulation Studies (COMPASS) forcefield [55] was used to describe all intra- and inter-molecular interactions. The COMPASS forcefield has the form:

$$E = E_b + E_\theta + E_\varphi + E_\chi + E_{b,b'} + E_{b,\theta} + E_{b,\varphi} + E_{\theta,\varphi} + E_{elec} + E_{LJ} = \Sigma_b[k_2(b - b_0)^2 + k_3(b - b_0)^3 + k_4(b - b_0)^4] + \Sigma_\theta[k_2(\theta - \theta_0)^2 + k_3(\theta - \theta_0)^3 + k_4(\theta - \theta_0)^4] + \Sigma_\varphi[k_1(1 - \cos\varphi) + k_2(1 - \cos2\varphi) + k_3(1 - \cos3\varphi)] + \Sigma_\chi k_2\chi^2 + \Sigma_{b,b'k}(b - b_0)(b' - b'_0) + \Sigma_{b,\theta k}(b - b_0)(\theta - \theta_0) + \Sigma_{b,\varphi}(b - b_0)[k_1\cos\varphi + k_2\cos2\varphi + k_3\cos3\varphi] + \Sigma_{\theta,\varphi}(\theta - \theta_0)[k_1\cos\varphi + k_2\cos2\varphi + k_3\cos3\varphi] + \Sigma_{\theta,\theta,\varphi k}(\theta' - \theta'_0)(\theta - \theta_0)\cos\varphi + \Sigma_{i,j}(q_iq_j)/r_{ij} + \Sigma_{i,j}\varepsilon_{ij}\,[2(\sigma_{ij}/r_{ij})^9 - 3(\sigma ij/rij)^6] \quad (1)$$

wherein E_b, E_θ, E_φ, and E_χ are, respectively, contributions from bond (b) stretching, angle (θ) bending, torsional angle (φ) twisting, and out-of-plane angle (χ) distortion. The terms $E_{b,b'}$, $E_{b,\theta}$, $E_{b,\varphi}$, and $E_{\theta,\varphi}$ are cross-coupling terms between internal coordinates. E_{elec} and E_{LJ} are non-bonded interaction terms accounting for electrostatic and dispersive van der Waals forces, respectively. The equilibrium bond length, bond angle, and torsional angle are denoted by b_0, θ_0, and φ, respectively. The terms k, k_1, k_2, and k_3 are coefficients specific to the COMPASS forcefield. For the non-bonded interactions, q is the magnitude of the electric charge of an atom, rij is the separation between sites i and j, and ε and σ are the Lennard-Jones parameters. It may be noted that the MOF adsorbent structure was rigid in the MC simulations; hence, all terms to do with bond bending, etc., only apply to the adsorbate molecules. The COMPASS forcefield contains numerous terms to account for all of the energetic contributions described in Equation (1), and the reader is referred to the MCCCS Towhee project [56], which contains a significant collection of the publicly available terms for this proprietary forcefield.

An analytical tail correction was used for the van der Waals interactions beyond a cut-off radius of 1.5 nm. To accurately account for the electrostatic interactions of the particles in the system, the Ewald summation technique was employed [57]. In the context of the COMPASS force field, van der Waals interactions are described using a 9-6 Lennard-Jones potential [58] coupled with the Waldman–Hagler combining rules [59] for unlike interactions. The COMPASS force field has been successfully used to describe a range of metal–organic frameworks (including those with open-metal sites) [60–64] as well as the gas components of interest [65–68]; hence, it was selected for this study. It may be noted that the limitations of the molecular model include simplifying assumptions used to develop functional forms for the bonded and non-bonded interactions.

To avoid artificial periodicity [69], it may be necessary to ensure a minimum size of the simulation cell such that the length of each side is at least twice the cut-off radius. This is a general problem potentially affecting any system being simulated at the molecular level. However, it can be noted that, for some systems, periodicity artefacts may be negligible if the simulation cell is sufficiently large, such as for clathrate hydrates [70], cement hydrate [66], and montmorillonite [71], wherein the aforementioned studies demonstrated that convergence in terms of adsorption could occur for these systems despite the length of each side of a simulation cell being less than twice the cut-off radius. Hence, tests were performed using carbon dioxide as the adsorbate to assess the adsorption at the temperature of interest (298 K) as a function of fugacity for simulation cells consisting of $1 \times 1 \times 1$, $1 \times 1 \times 2$, and $1 \times 1 \times 4$ unit cells. It was found that a single unit cell was sufficient to describe the CaMOF adsorbent. Additional tests were conducted to assess the effect of the cut-off radius, wherein the cut-off radius was both decreased and increased, and it was observed that any effects in terms of adsorption converged for a cut-off radius of 1.5 nm. It may be noted here that the metal–organic framework has a unit cell with parameters a = 3.18746 nm, b = 3.18746 nm, c = 0.89890 nm, $\alpha = \beta = 90.0°$, and $\gamma = 120°$. The results of these tests can be found in the Supplementary Materials.

A useful property in terms of assessing the practicalities of implementing the proposed adsorption system is the isosteric heat of adsorption. The isosteric heat can be considered as a function of the loading of the adsorbent to determine the regenerability of the adsorbent [72]. The higher the magnitude of h_{ad}, the higher the energy costs for regeneration of the adsorbent. The isosteric heat of adsorption was computed from the adsorption isotherm results generated via Monte Carlo molecular simulation using the Clapeyron equation:

$$h_{ad} = RT\,[d(\ln P)/d(\ln T)] \quad (2)$$

As with the adsorption isotherms, the isosteric heats of adsorption were averaged across three independent simulations at ambient temperature (i.e., T = 298 K).

In addition to Monte Carlo molecular simulations, the diffusivity of all pure gas species in CaMOF was estimated using molecular dynamics, following a procedure in the literature for MOFs [73]. Dynamical simulations in the canonical NVT ensemble at 298 K were performed with periodic boundary conditions using a 1 × 1 × 4 supercell with dimensions of 3.18746 × 3.18746 × 3.55956 nm, which was packed with a number of molecules of each gas species equivalent to their absolute loading at 100 kPa to compute pure species diffusivity. This supercell had the chemical formula $C_{648}H_{720}N_{360}O_{216}Ca_{72}$. The Nosé–Hoover thermostat [74,75] was used to maintain the temperature of the system, and the velocity Verlet algorithm [76] with a timestep of 1 fs was utilised. As per the procedure described in the literature [73], 1 ns was used to equilibrate the system, after which 5 ns was used to generate data with configurational sampling every 100 fs. The self-diffusion coefficient D was then obtained from a linear fit of the mean squared displacement (MSD) according to Einstein's relation [77] using an interval of no less than 1 ns:

$$D = (1/6)\lim_{\Delta t \to \infty} d(MSD)/d(\Delta t) \quad (3)$$

All pure species adsorption isotherms were assessed in terms of the most widely used two-parameter adsorption isotherm models, namely, those of Langmuir [78] and Freundlich [79]. The Langmuir adsorption isotherm model is possibly the simplest means of describing gas or liquid adsorption onto a substrate and is based on the following assumptions: monolayer adsorption, no lateral interaction or steric hindrance between adsorbed molecules, and identical and equivalent adsorption sites that are finite and localised. Mathematically, the Langmuir model is typically given as

$$q = Qb_{Langmuir}P/(1 + b_{Langmuir}P) \quad (4)$$

in which q is the quantity of gas adsorbed, P is the gas pressure, Q is the saturation adsorption capacity, and $b_{Langmuir}$ is the so-called Langmuir equilibrium constant. The Freundlich model accounts for reversible and non-ideal adsorption, while also factoring in the non-uniform distribution of adsorption affinities and heats across heterogeneous surfaces. It is presented as

$$q = KP^{(1/n)} \quad (5)$$

wherein K is the Freundlich constant describing the adsorption capacity and 1/n represents the degree of heterogeneity of the surface. Another two-parameter model that was considered was the Temkin adsorption isotherm model [80]:

$$q = b_{Temkin} \ln (AP) \quad (6)$$

in which b_{Temkin} accounts for the total quantity adsorbed, and A describes the pressure-sensitivity of adsorption. This model ignores extreme lows and highs of pressure and assumes that the heat of adsorption of all molecules decreases linearly rather than logarithmically with respect to adsorption coverage. The Temkin model is characterised by a uniform distribution of binding energies.

In addition to the two-parameter Langmuir, Freundlich, and Temkin models of adsorption, the Redlich–Peterson [81] and Sips [82] isotherms were also considered. The Redlich–Peterson isotherm is a hybrid isotherm that incorporates features of both the Langmuir and Freundlich approaches; at low pressures, it resembles the Langmuir model, while at high pressures, it approaches the Freundlich isotherm, as given by:

$$q = kP/(1 + aP^{b'}) \quad (7)$$

in which k/a indicates the adsorption capacity, while b′ is a constant indicating deviation from the simplistic Langmuir description (for which b′ = 1).

The Sips adsorption isotherm is also a combination of the Langmuir and Freundlich isotherms, which was developed to describe heterogeneous adsorption systems while circumventing the limitation of increasing adsorbate concentrations associated with the Freundlich isotherm. At low pressures, it reduces to the Freundlich isotherm, while at high pressures, it results in monolayer adsorption characteristic of the Langmuir model. The Sips model is given by:

$$q = kP^{bSips}/(1 + aP^{bSips}) \quad (8)$$

in which k/a indicates the adsorption capacity, while b_{Sips} is a constant indicating deviation from the simplistic Langmuir description (for which $b_{Sips} = 1$). Note that fitting was undertaken using nonlinear least squares regression, as implemented in GNU Octave version 5.2.0 [83].

Assuming ideal mixture behaviour and non-competitive sorption, a batch equilibrium model [84] of the biogas upgrading system can be applied to this context—the reader is referred to the literature [85] for a detailed discussion regarding the computational aspects of this approach. The main limitation of the batch equilibrium approach is, of course, that it assumes equilibrium to have been reached. Hence, it illustrates the best-case performance of an adsorption system. Essentially, a material balance is solved across both the charging and discharging phases of a single adsorption bed. For vacuum swing adsorption (VSA), the following material balances need to be solved simultaneously:

$$n_i^{in} = n_i^{ad} + Wq_i^{ad} \quad (9)$$

$$n_i^{ad} + Wq_i^{ad} = n_i^{de} + Wq_i^{de} + n_i^{out} \quad (10)$$

in which n_i^{in} is the number of moles of species i entering the system, n_i^{ad} is the number of moles in the gas phase in equilibrium with the adsorbed phase Wq_i^{ad} during the pressurisation step, n_i^{de} is the number of moles in the gas phase in equilibrium with the adsorbed phase Wq_i^{de} during desorption, and n_i^{out} is the number of moles in the discharge stream.

3. Results

3.1. Pure Species Adsorption Behaviour

Figure 2 shows the absolute adsorption isotherms for pure carbon dioxide, nitrogen, methane, oxygen, hydrogen sulphide, and hydrogen in the CaMOF at ambient temperature (i.e., 298 K) generated by Monte Carlo molecular simulations in the grand canonical ensemble. The results of the fitted adsorption isotherms are presented in Tables 2–6. Pure species experimental data for carbon dioxide and methane from the literature [30] are also included, although measurements for the other species are lacking. It is apparent that the adsorbent possesses a large adsorption capacity for H_2S and CO_2 over the conditions of interest, with potentially high selectivity for H_2S over CO_2. This feature suggests that the CaMOF may have reduced effectiveness in terms of reducing carbon emissions for biogas containing substantial quantities of hydrogen sulphide, which may impact process design work. It is also clear that CaMOF does not adsorb H_2 significantly over the range of conditions of interest to this study, suggesting that this material may be useful for hydrogen-processing applications, at least when H_2 occurs in conjunction with biogas constituents. Regarding the present study, the low uptake of hydrogen combined with the high uptake of CO_2 and H_2S suggests that using CaMOF to pre-treat biogas may result in a cleaner biogas product with lower carbon and sulphur emissions. It is apparent that the COMPASS forcefield consistently overestimates the CO_2 uptake by a factor of about 2.27, whereas it underestimates the adsorption of methane by a factor of about 6.03. With these empirical factors applied to the adsorption isotherms (functionally, this would have the form $q' = Fq$ where F is the appropriate factor), the computed adsorption isotherms match the available experimental data favourably. It can be noted that despite the deviations, the shapes of the adsorption isotherm curves for both methane and carbon dioxide are qualitatively similar to the experimental data. Hence, while the assumptions behind the self-consistent

COMPASS force field may have some limitations for biogas constituent interactions with this particular CaMOF, qualitative observations and, thus, physical behaviour should be consistent with experimental observations, especially given that COMPASS has been used successfully for various MOFs and biogas components in other contexts, as outlined in Section 2. The deviation present may indicate that in this specific system, corrections such as, for example, steric adjustments may need to be undertaken for this forcefield on account of the approximately constant ratio between the experimental and simulation results in terms of sorption.

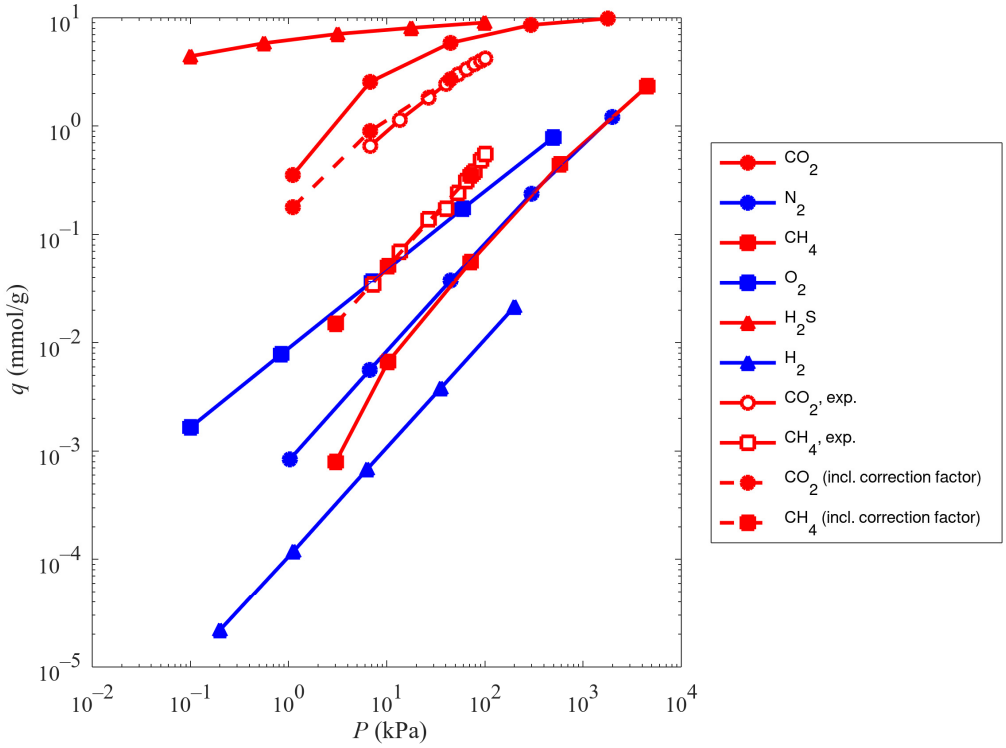

Figure 2. Pure species adsorption isotherms for biogas constituents in CaMOF. Where they are not visible, the error bars (representing the standard deviation) are smaller than the symbols. The lines are guides for the eye. The open symbols represent experimental data [30] and the dashed line series represents an adjustment of the adsorption isotherms using a simple empirical factor, as outlined in the text.

With respect to carbon dioxide, a comparison between the adsorption isotherm models with the strongest correlation to experimental data (i.e., the Langmuir and Sips models) may be undertaken using the Akaike information criterion, AIC [86], adjusted for small sample sizes [87] (AICc). In this case, the most likely model to describe the results of the simulations would be the Langmuir model, given that it has an AICc of 14.356 compared to 36.764 for the Sips model. These values suggest that the Sips model is approximately 1.4×10^{-5} times as probable as the Langmuir model. For methane, it is clear that the best fit among the adsorption isotherm models is the Langmuir model, since its correlation coefficient is practically unity. Experimental measurements [30] for methane and carbon dioxide over much narrower pressure ranges yielded behaviour incorporating features of both the Langmuir and Freundlich adsorption isotherm models. It can be noted that in this study, strictly employing the correlation coefficient as a measure of the goodness of fit would result in the Sips model being selected over the Langmuir model on account of its higher R^2 value; however, the Akaike information criterion suggests that it may, in fact, be overfitting the data, as the Sips model is only about 0.013 times as probable as the Langmuir model. An outcome of these analyses for carbon dioxide and methane is that

the adsorption sites are likely homogeneous, since this is a key assumption underlying the Langmuir adsorption isotherm model.

In terms of fitting adsorption isotherm models to the data for H_2S, it may be preferable to select either the Redlich–Peterson or Sips models. Purely on the basis of the R^2 as the value for comparison, the better choice would be the Sips model. However, computing the AICc for these adsorption isotherm models yields the following values for the Redlich–Peterson and Sips models, respectively: 40.5, and 41.7. Hence, the optimal model to select in terms of both agreeing with the results and minimising overfitting is the Redlich–Peterson model. On the basis of AICc, the Sips model is 0.54 times as probable as the Redlich-Peterson model. This suggests that the adsorption of hydrogen sulphide on the CaMOF adsorbent has features of both the Langmuir and Freundlich isotherms, tending to Langmuir-type behaviour at low pressure with greater site heterogeneity at high pressures as it shifts towards Freundlich-type behaviour.

Table 2. Fitted parameters and correlation coefficient (R^2) for the Langmuir model based on the results of grand canonical Monte Carlo simulations at T = 298 K.

Component	$b_{Langmuir}$ (1/kPa)	Q (mmol/g)	R^2
Methane	$1.291 \times 10^{-4} \pm 2.016 \times 10^{-6}$	$6.362 \pm 6.411 \times 10^{-2}$	1.000
Carbon dioxide	$3.972 \times 10^{-2} \pm 7.483 \times 10^{-3}$	9.634 ± 0.357	0.992
Nitrogen	$1.870 \times 10^{-4} \pm 7.687 \times 10^{-7}$	4.492 ± 0.0136	1.000
Oxygen	$2.249 \times 10^{-3} \pm 2.664 \times 10^{-4}$	$1.487 \pm 8.796 \times 10^{-2}$	1.000
Hydrogen	$1.018 \times 10^{-3} \pm 6.503 \times 10^{-4}$	$0.126 \pm 6.721 \times 10^{-2}$	0.999
Hydrogen sulphide	9.254 ± 4.321	8.022 ± 0.545	0.807

Table 3. Fitted parameters and correlation coefficient (R^2) for the Freundlich model based on the results of grand canonical Monte Carlo simulations at T = 298 K.

Component	K (mmol/g)	n	R^2
Methane	$2.331 \times 10^{-3} \pm 3.141 \times 10^{-4}$	$1.217 \pm 2.391 \times 10^{-2}$	1.000
Carbon dioxide	2.057 ± 0.793	4.528 ± 1.224	0.893
Nitrogen	$1.651 \times 10^{-3} \pm 1.315 \times 10^{-4}$	$1.150 \pm 1.400 \times 10^{-2}$	1.000
Oxygen	$9.353 \times 10^{-3} \pm 1.060 \times 10^{-4}$	$1.402 \pm 3.638 \times 10^{-3}$	1.000
Hydrogen	$1.064 \times 10^{-4} \pm 3.094 \times 10^{-7}$	$0.998 \pm 5.512 \times 10^{-4}$	1.000
Hydrogen sulphide	6.029 ± 0.202	10.608 ± 1.183	0.968

Table 4. Fitted parameters and correlation coefficient (R^2) for the Redlich–Peterson model based on the results of grand canonical Monte Carlo simulations at T = 298 K.

Component	k (mmol/g·kPa)	a (1/kPa$^{b'}$)	b′	R^2
Methane	$1.443 \times 10^{-4} \pm 2.726 \times 10^{-4}$	-1.075 ± 0.189	$-4.718 \times 10^{-2} \pm 0.107$	0.999
Carbon dioxide	$2.465 \times 10^{-3} \pm 2.887 \times 10^{-2}$	-1.601 ± 11.468	-0.129 ± 1.950	0.681
Nitrogen	$1.980 \times 10^{-4} \pm 3.693 \times 10^{-4}$	$-0.962 \pm 4.608 \times 10^{-2}$	$-4.613 \times 10^{-2} \pm 0.116$	1.000
Oxygen	$1.148 \times 10^{-2} \pm 5.926 \times 10^{-3}$	0.674 ± 0.599	$0.360 \pm 4.746 \times 10^{-2}$	1.000
Hydrogen	$1.058 \times 10^{-4} \pm 1.113 \times 10^{-5}$	$-7.491 \times 10^{-3} \pm 8.895 \times 10^{-2}$	0.159 ± 1.120	1.000
Hydrogen sulphide	214.420 ± 39.366	32.878 ± 6.465	$0.928 \pm 5.007 \times 10^{-3}$	0.998

In terms of diffusion behaviour, it was difficult to discern trends in terms of the molecular properties of the gas species and the estimated diffusivity. When considering the molecular mass of the gas species, it was observed that the diffusivity generally decreased with increasing gas molecule mass, which is largely expected based on the kinetic behaviour of fluid species. This trend was not linear, however, and there may be steric effects related to the size and shape of gas molecules as well as the size and shape of channels within the CaMOF. Comparing the magnitudes of the diffusivities yields the following ranking in

terms of rates of diffusion in the MOF: $H_2 > N_2 > O_2 > CO_2 > CH_4 > H_2S$. The ranking of affinities in terms of adsorption (considering pressures from 10 kPa upwards) is $H_2S > CO_2 > O_2 > N_2 > CH_4 > H_2$. Comparing these two rankings as well as the results in Figure 3 suggests that it may not be straightforward to predict the diffusion of biogas constituents in CaMOF based solely on the quantity of gas adsorbed or a simplistic measure such as a single molecular property.

Table 5. Fitted parameters and correlation coefficient (R^2) for the Temkin model based on the results of grand canonical Monte Carlo simulations at T = 298 K.

Component	b (mmol/g)	A (1/kPa)	R^2
Methane	$2.331 \times 10^{-3} \pm 3.141 \times 10^{-4}$	$1.217 \pm 2.391 \times 10^{-2}$	0.698
Carbon dioxide	1.350 ± 0.098	1.264 ± 0.440	0.985
Nitrogen	0.141 ± 0.059	0.187 ± 0.269	0.653
Oxygen	$8.140 \times 10^{-2} \pm 3.281 \times 10^{-2}$	1.669 ± 2.618	0.672
Hydrogen	$2.707 \times 10^{-3} \pm 1.176 \times 10^{-3}$	1.094 ± 1.481	0.639
Hydrogen sulphide	$0.665 \pm 2.230 \times 10^{-2}$	9971.3 ± 5324.8	0.993

Table 6. Fitted parameters and correlation coefficient (R^2) for the Sips model based on the results of grand canonical Monte Carlo simulations at T = 298 K.

Component	k (mmol/g·kPa^b)	b	a (1/kPa^b)	R^2
Methane	$3.514 \times 10^{-2} \pm 3.842 \times 10^{-2}$	0.260 ± 0.347	$-9.770 \times 10^{-2} \pm 0.313$	0.996
Carbon dioxide	0.682 ± 0.180	$0.793 \pm 8.732 \times 10^{-2}$	$6.730 \times 10^{-2} \pm 1.652 \times 10^{-2}$	0.998
Nitrogen	$2.412 \times 10^{-2} \pm 1.303 \times 10^{-2}$	0.202 ± 0.370	-0.196 ± 0.597	0.996
Oxygen	$1.900 \times 10^{-2} \pm 8.334 \times 10^{-3}$	0.477 ± 0.162	$-2.738 \times 10^{-2} \pm 4.182 \times 10^{-2}$	0.999
Hydrogen	$5.356 \times 10^{-4} \pm 2.041 \times 10^{-4}$	0.316 ± 0.341	-0.162 ± 0.331	0.998
Hydrogen sulphide	14.856 ± 1.095	$0.290 \pm 2.553 \times 10^{-2}$	1.387 ± 0.160	0.999

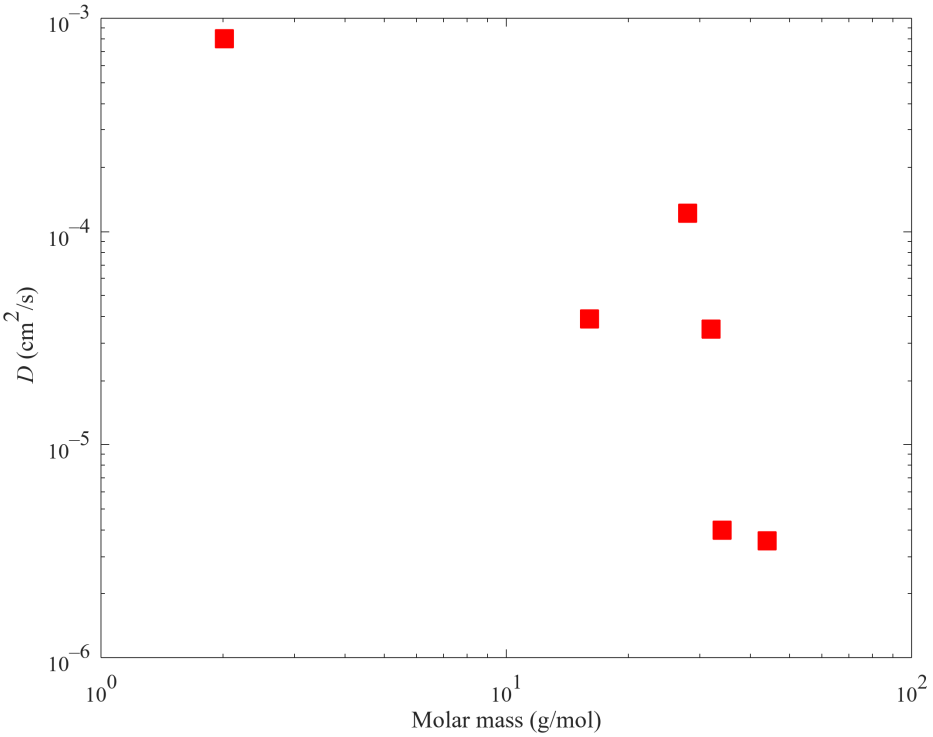

Figure 3. Diffusivity plotted as a function of the molar mass of each gas species.

3.2. Isosteric Heat of Adsorption

Figure 4 shows the heats of adsorption for all species computed from the results of the pure species Monte Carlo molecular simulations. It is apparent that the CaMOF adsorbent is not well suited to remove CO_2 as the energy costs of regeneration tend to increase as the quantity of carbon dioxide adsorbed increases, whereas the heat of adsorption of nitrogen does not vary with respect to the amount of gas adsorbed. While the trend for hydrogen sulphide is that of a rapid decrease in terms of the heat of adsorption with respect to gas uptake, the magnitude of h_{ad} is rather high at 57 to 68 kJ/mol over the range of conditions considered in this study. The energy costs of regeneration in this study refer to the amount of energy needed to release the adsorbed gas molecules from CaMOF adsorbent regenerating the adsorbent for reuse. One of the key factors influencing these energy costs is the heat of adsorption. Higher h_{ad} leads to stronger interactions between the adsorbent and the adsorbed gas molecules. This means that more energy will be required to release the gas molecules during regeneration processes. For comparison, the heat of adsorption of CO_2 varied from 29 to 40 kJ/mol in this study, while a previous report [72] on a favourable adsorbent in terms of regenerability yielded an isosteric heat of adsorption of approximately 20 kJ/mol for carbon dioxide on a different MOF-based adsorbent. The increase in h_{ad} with the increase in the amount of CO_2 adsorbed implies that as the CO_2 is adsorbed, it becomes difficult and energetically expensive to desorb it. This also applies to the adsorption of H_2S, because the h_{ad} of H_2S is high, which implies that regenerating adsorbent for H_2S removal will be energy-intensive. The adsorption heat effect impacts not only the energy required for regenerating the adsorbent, but also the initial adsorption capacity and efficiency. As seen in the case of H_2S, the heat of adsorption decreases with the increase in gas uptake, which may cause the adsorbent to become less efficient at higher gas concentrations. Hence, it can be expected that regenerability issues may be encountered when employing CaMOF in industrial operations, and overcoming this problem may increase the energetic costs of the gas separation process.

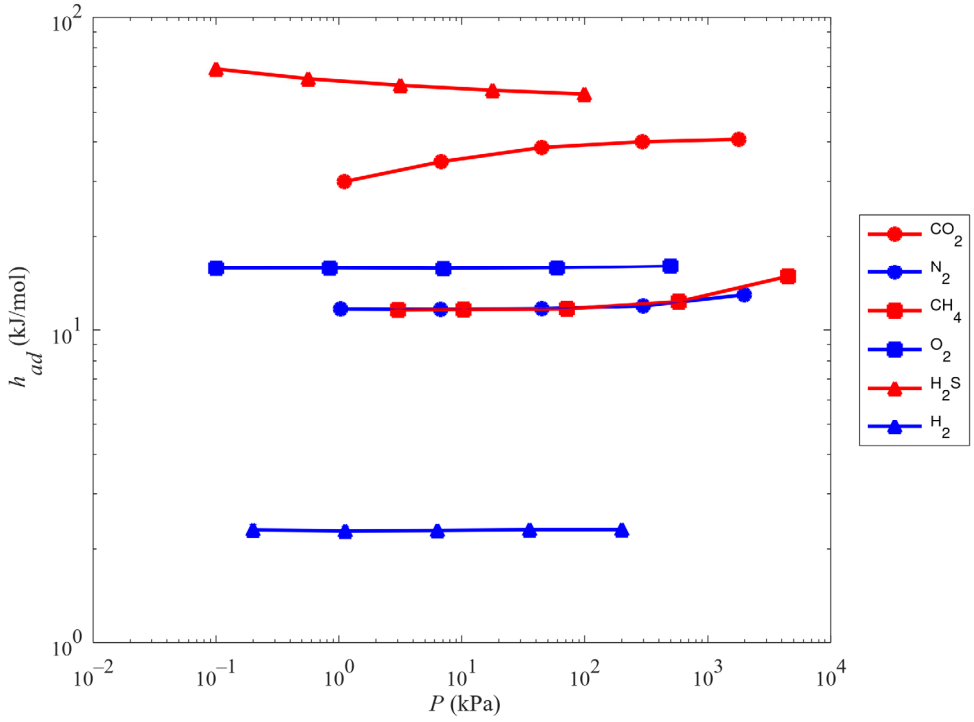

Figure 4. Pure species isosteric heats of adsorption (h_{ad}) in the Ca-MOF adsorbent.

3.3. Mixture Sorption

Figure 5 shows the uptake of all biogas constituents on CaMOF for a typical biogas composed of 30 mol-% CO_2, 14.99 mol-% N_2, 50 mol-% CH_4, 3 mol-% O_2, 0.01 mol-% H_2S, and 2 mol-% H_2 [5] in terms of absolute adsorption. It is apparent that for the enhanced selectivity of hydrogen sulphide and carbon dioxide, the vacuum pressure operation of pressure swing adsorption systems would be preferred. In terms of non-calorific species selectivity—defined as $S = (\Sigma x_{\text{non-calorific}}/\Sigma y_{\text{non-calorific}})/(\Sigma x_{\text{calorific}}/\Sigma y_{\text{calorific}})$, where x is the mole fraction of the relevant species in the adsorbed phase—optimal selectivity (S = 121) to remove the non-calorific species was observed at 1000 kPa, with a decreasing trend both below and above this pressure. However, the selectivity in favour of the adsorption of non-calorific species was higher at 10 kPa (where S = 98) than at 10^4 kPa. It can be noted that, in terms of the selectivity of a specific species i with respect to CH_4, the expression for S would be defined as $S = (x_i/y_i)/(x_{CH4}/y_{CH4})$.

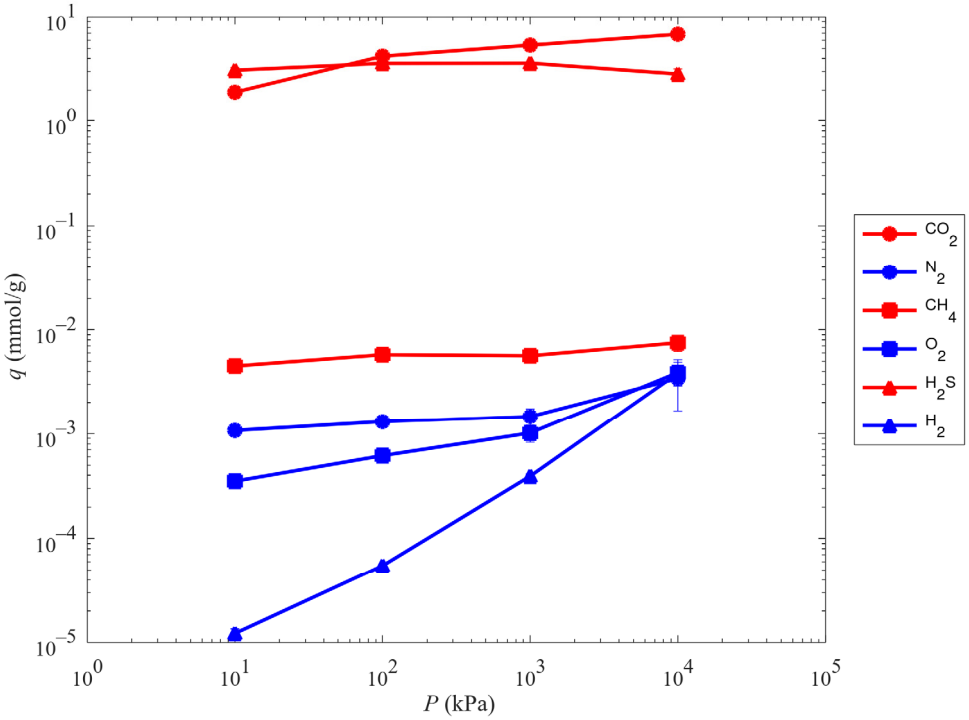

Figure 5. Mixture adsorption isotherms for biogas constituents in Ca-MOF for biogas composed of 30 mol-% CO_2, 14.99 mol-% N_2, 50 mol-% CH_4, 3 mol-% O_2, 0.01 mol-% H_2S, and 2 mol-% H_2. Where they are not visible, the error bars (representing the standard deviation) are smaller than the symbols. The lines are guides for the eye.

An additional biogas feedstock was also considered, as shown in Figure 6. This feed gas had a composition of 30 mol-% CO_2, 14.9 mol-% N_2, 50 mol-% CH_4, 3 mol-% O_2, 0.1 mol-% H_2S, and 2 mol-% H_2 [5], therefore possessing a higher proportion of sour gas constituents. The selectivity trends were similar to the previous biogas feedstock, with a peak selectivity in favour of non-calorific species of 128 at 1000 kPa, which decreased to 87 by 10^4 kPa and to 111 at 10 kPa. It is apparent then that a higher fraction of hydrogen sulphide in the biogas may make the performance of biogas cleaning via CaMOF less sensitive to pressure changes, especially below 1000 kPa. Altogether, both sets of multicomponent molecular simulations suggest that low-pressure or vacuum-pressure operation is desirable for the purposes of cleaning biogas using CaMOF on account of the high selectivity observed for non-calorific species, as well as the relatively low sensitivity to pressure changes and the magnitude of the uptake of the dominant species (i.e., methane and carbon dioxide).

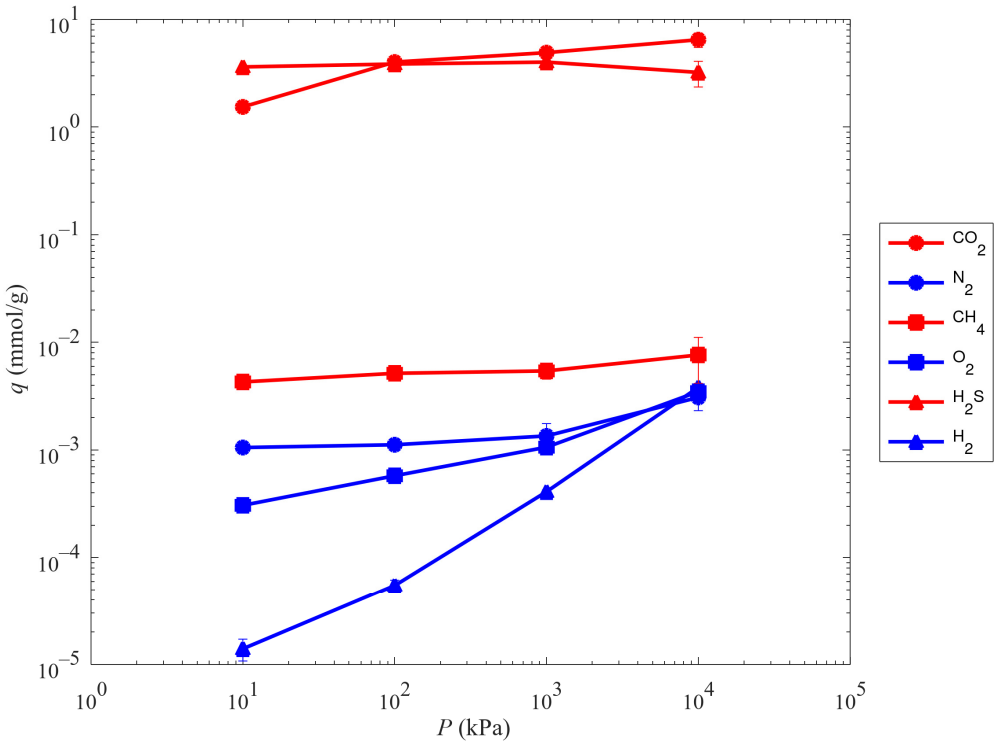

Figure 6. Mixture adsorption isotherms for biogas constituents in Ca-MOF for biogas composed of 30 mol-% CO_2, 14.9 mol-% N_2, 50 mol-% CH_4, 3 mol-% O_2, 0.1 mol-% H_2S, and 2 mol-% H_2. Where they are not visible, the error bars (representing the standard deviation) are smaller than the symbols. The lines are guides for the eye.

The observed selectivity behaviour at peak adsorbent loading can be compared with several other adsorbents proposed for biogas purification, as outlined in Table 7. It is evident that CaMOF shows some potential for separating both H_2S and CO_2 from methane on account of it possessing substantial selectivity for hydrogen sulphide compared to other adsorbents that have been proposed and studied for this task. As stated previously, a significant limitation of the present study is its in silico nature, although the results suggest that proceeding with laboratory experiments may be a fruitful venture. However, the strength of the forces between H_2S and the CaMOF, especially at low pressures, should be considered. In this regard, Figures 4 and 5 show that the adsorption sites of hydrogen sulphide at low pressure are strongly attractive, much more so than for CO_2. This suggests that the regeneration of adsorption beds may be challenging when such systems are employed to remove hydrogen sulphide from biogas.

Table 7. Comparison of CaMOF selectivity with other adsorbent materials for the purpose of biogas purification. * These values are the selectivity factor q_{CO2}/q_{CH4}.

Adsorbent	$S_{H2S/CH4}$	$S_{CO2/CH4}$	Conditions	Feed Gas Composition	Reference
CaMOF	3.4×10^5	35	298 K, 10 kPa	30 mol-% CO_2, 14.99 mol-% N_2, 50 mol-% CH_4, 3 mol-% O_2, 0.001 mol-% H_2S, 2 mol-% H_2	This study

Table 7. *Cont.*

Adsorbent	$S_{H2S/CH4}$	$S_{CO2/CH4}$	Conditions	Feed Gas Composition	Reference
	4.2×10^5	30	298 K, 10 kPa	30 mol-% CO_2, 14.9 mol-% N_2, 50 mol-% CH_4, 3 mol-% O_2, 0.01 mol-% H_2S, 2 mol-% H_2	This study
CaMOF	-	16.5	298 K, 100 kPa	50 mol-% CH_4, 50 mol-% CO_2	[30]
Resorcinol–formaldehyde carbon xerogel	-	2.38	303 K, 100 kPa	50 mol-% CH_4, 50 mol-% CO_2	[88]
6FDA-DAM polyimide	11	5.4	308 K, 690 kPa	60 mol-% CH_4, 20 mol-% CO_2, 20 mol-% H_2S	[89]
Fluorinated MOF NbOFFIVE-1-Na/6FDA-DAM polyimide mixed matrix	10	5.3	308 K, 690 kPa	60 mol-% CH_4, 20 mol-% CO_2, 20 mol-% H_2S	[89]
Fluorinated MOF AlOFFIVE-1-Na/6FDA-DAM polyimide mixed matrix	10	4.5	308 K, 690 kPa	60 mol-% CH_4, 20 mol-% CO_2, 20 mol-% H_2S	[89]
CuMOF	-	5.9 *	303 K, 10 kPa	-	[90]
Zeolite 13X	-	8.4 *	303 K, 110 kPa	-	[91]
Melamine-based covalent organic framework/MOF heterostructure	-	44.2	298 K 200 kPa	70 vol-% CH_4, 30 vol-% CO_2	[92]
OH-functionalised MOF	-	17.2	273 K, 101.3 kPa	Henry's law (i.e., $p_i \rightarrow 0$)	[93]
Cu-BTC MOF	-	11.5	303 K, 10^3 kPa	75 mol-% CO_2, 25 mol-% CH_4	[94]

4. Discussion

Firstly, the hydrogen sulphide sorption behaviour should be discussed. Figure 7 shows the density field of H_2S (at 298 K and the highest pressure considered for hydrogen sulphide in this study, namely, 99.22 kPa) in the CaMOF lattice. It is apparent that there may be multiple types of hydrogen sulphide adsorption sites as there are sites located near Ca, N, and O atoms. This observation alone suggests that an adsorption isotherm model accounting for site heterogeneity such as the Freundlich model, or possibly a model incorporating its features such as the Redlich–Peterson model, would most accurately describe hydrogen sulphide adsorption in the CaMOF adsorbent. It may be noted, however, that it may be more likely that there are adsorption sites at the channel vertices where Ca and N atoms are located. The adsorption isotherm analysis presented in Section 3.1 would concur with this visual assessment, as it was observed that the best fit for H_2S adsorption was obtained using the Redlich–Peterson mode, which has features of both the Langmuir and Freundlich isotherms, tending to Langmuir-type behaviour at low pressure with greater site heterogeneity at high pressures as it shifts towards Freundlich-type behaviour. An examination of the energy distribution for H_2S adsorbed in CaMOF, as shown in Figure 7, may be instructive in this regard.

Figure 8 shows three adsorption site types for H_2S defined in terms of the potential energy associated with them: −75 to −73 kJ/mol, −50 to −47 kJ/mol, and −32 to −30 kJ/mol. The latter two adsorption site types appear to be hard to distinguish at lower pressures, as evidenced by the significant degree of overlap between the energy distribution curves shown in Figure 4; this difficulty in distinguishing between the two higher energy sites is evident in the density field of adsorbed H_2S molecules shown in Figure 4. The first of

the identified adsorption site types (that are associated with a potential energy of −75 to −73 kJ/mol) may be related to the previously identified Ca/N regions of high affinity for H_2S sorption. The change in the probability density of the different peaks shown in Figure 5 demonstrates the difficulties in determining the adsorption behaviour in terms of simplistic adsorption isotherm models such as the Langmuir and Freundlich models. The results suggest that, at low pressures (below 18 kPa), there may effectively be only one accessible type of adsorption site for H_2S molecules, whereas at higher pressures, the shift is from one type of adsorption site to two site types at intermediate pressures (as shown by the clear distinction between the peaks at −75 to −73 kJ/mol and −50 to −47 kJ/mol at pressures from 18 kPa up to about 99 kPa), and then towards three site types from about 18 kPa onwards as the third energetic site type (associated with the peak at −32 to −30 kJ/mol) becomes noticeable. In terms of what this means in practical terms, if the modification or pre-treatment of the CaMOF is undertaken, the H_2S sorption capacity of the adsorbent at predetermined pressure values can be tailored to some extent by targeting the different adsorption sites.

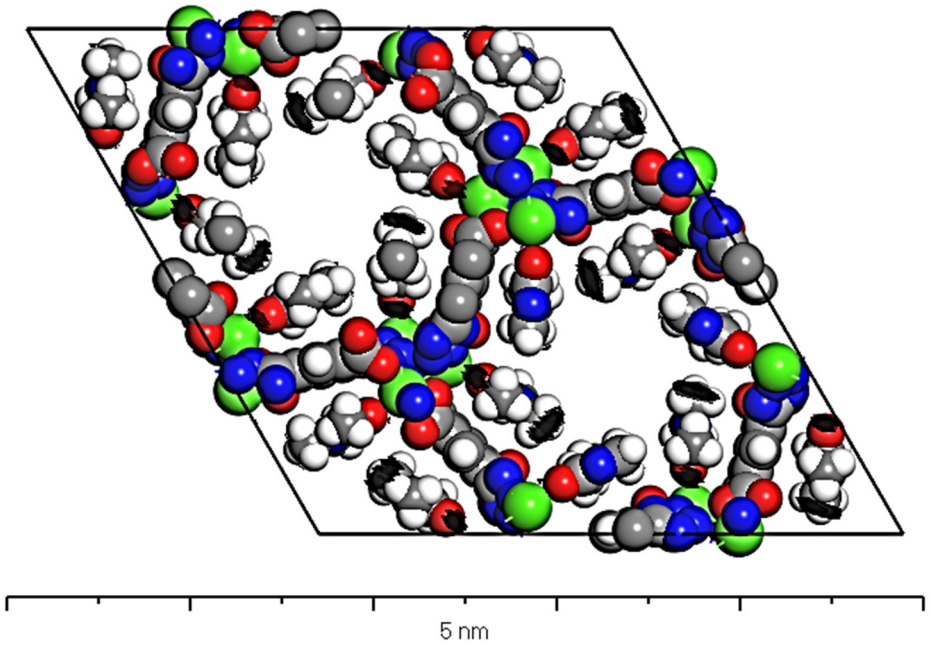

Figure 7. Density field of H_2S adsorbed onto the unit cell of the Ca-MOF at 298 K and 99.22 kPa. Atoms are colour-coded according to the element: white = hydrogen, grey = carbon, red = oxygen, blue = nitrogen, and green = calcium. Hydrogen sulphide-containing regions are indicated in black.

For comparison, the energy distributions of the next two most strongly adsorbed species, CO_2 and CH_4, are shown in Figures 9 and 10. For both species, it is apparent that increasing the gas pressure shifts the mean potential energy of the system, but in all cases, there remains a single energetic site type. Therefore, regardless of the pressure of the gas reservoir, the adsorption sites for a given pressure are homogeneous. This is in contrast to the case for hydrogen sulphide, where up to three energetic site types were observed. In terms of tailoring the CaMOF for targeted adsorption of carbon dioxide or methane, it is thus apparent that a single energetic site type needs to be considered, in contrast to the three site types observed for H_2S. It is suggested that work on the self-diffusion or binary diffusion of biogas constituents may be undertaken to probe gas–gas and gas–solid interactions from a dynamical perspective, which may complement the equilibrium-focussed work of the present study.

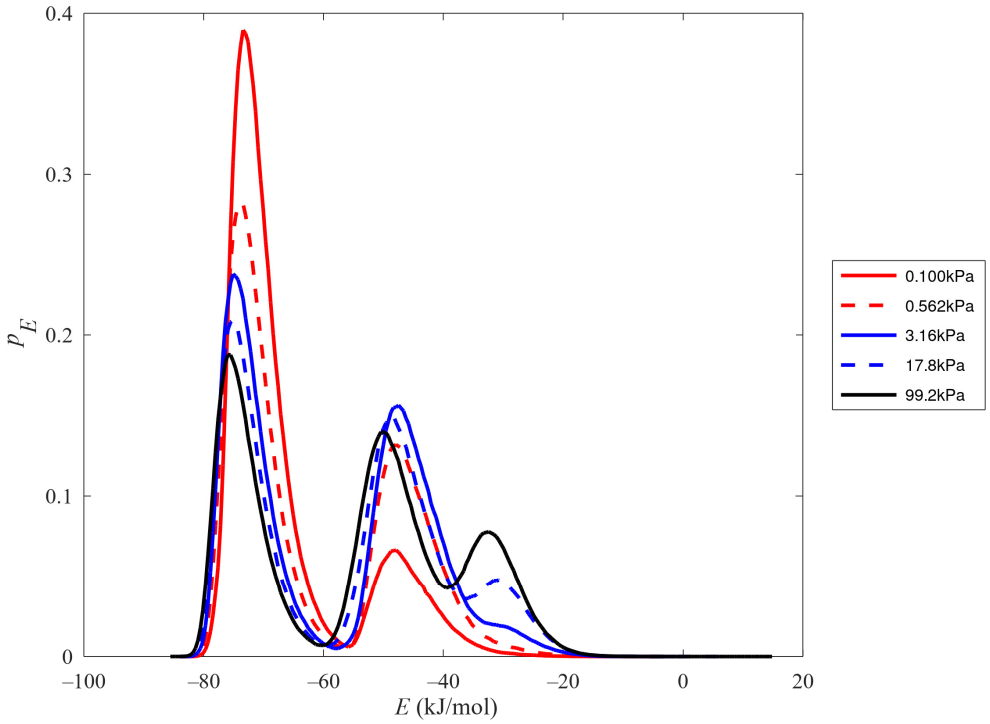

Figure 8. Energy distribution for H_2S adsorbed in CaMOF. E is the potential energy derived from configurations sampled during the grand canonical Monte Carlo simulations, and $p(E)$ is the probability of occurrence for each energy value. The lines are guides for the eye.

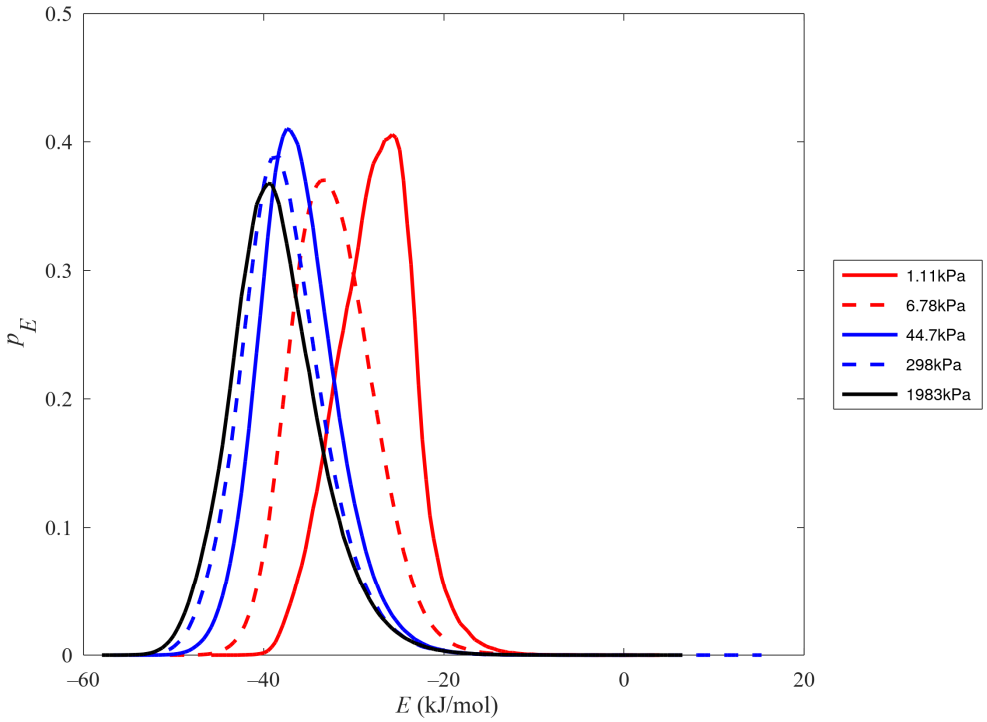

Figure 9. Energy distribution for CO_2 adsorbed in CaMOF. E is the potential energy derived from configurations sampled during the grand canonical Monte Carlo simulations, and $p(E)$ is the probability of occurrence for each energy value. The lines are guides for the eye.

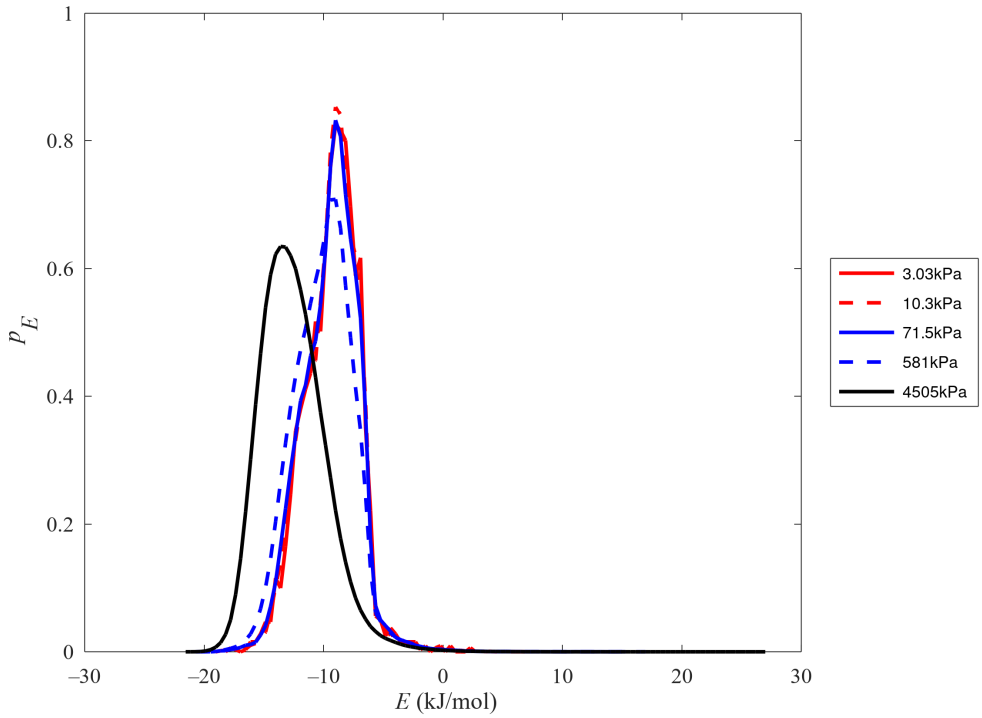

Figure 10. Energy distribution for CH_4 adsorbed in CaMOF. E is the potential energy derived from configurations sampled during the grand canonical Monte Carlo simulations, and $p(E)$ is the probability of occurrence for each energy value. The lines are guides for the eye.

In terms of potential design work, the results of the Monte Carlo simulations suggest that vacuum swing adsorption using CaMOF adsorbent may be pursued to yield a practicable gas separation system. Vacuum operation does, of course, entail its own challenges, such as higher capital costs for implementation, and a techno-economic assessment that balances capital and operating costs to determine the optimal vacuum pressure would be necessary [95]. That being said, a favourable selectivity in favour of non-calorific versus calorific gases at 10 kPa suggests a promising pathway to developing an effective biogas upgrading system. For example, a quick estimate of the mass of adsorbent containing all of the hydrogen sulphide in the biogas mixture referred to in Figure 7 yields quantities of about 0.05 to 0.06 g of adsorbent per mole of feed gas. Hence, producing cleaner-burning biogas without sulphur may require low capital costs by virtue of smaller adsorbent bed sizes. With reference to CO_2 removal, it is also then clear that very small bed sizes may be sufficient to produce purified biogas with a higher heating value.

Apart from upgrading the calorific value of biogas for use as a fuel, CaMOF may be incorporated into biogas reforming processes for the removal of carbon dioxide from feedstock as part of biogas upgrading; for the purposes of this study, solar-driven biogas steam reforming [96] will be used as a reference case study due to its recent active development. As shown in Figure 11, a key step in this process is biogas upgrading wherein a feedstock comprising 60 mol-% methane with carbon dioxide is separated to produce pure carbon dioxide and a stream rich in methane with a carbon dioxide residue. Adsorption typically entails low energy costs compared to many separation schemes, and it can therefore be helpful to consider a CaMOF-based pressure swing adsorption system for the purpose of biogas upgrading.

Note that W is the mass of the adsorption bed. Due to the selective adsorption of carbon dioxide by CaMOF, the gas discharged by the pressure swing adsorption unit described by Equations (8) and (9) would be rich in methane. Solving the simultaneous material balance over a range of conditions yields the results presented in Figure 12. To replicate the process conditions in the literature [96] as closely as possible for the purposes of integration with the solar biogas reforming process, a bed mass of about 30–42 g/mole of feed gas with

an operating pressure of approximately 70–78 kPa would be suitable for cleaning a gas mixture consisting of 60 mol-% methane with carbon dioxide. These conditions can yield a methane-rich stream comprising 93 mol-% methane and all of the methane that was in the feed, demonstrating that a CaMOF-based VSA system may be incorporated into a solar-driven biogas reforming process. It can be noted that the secondary outlet stream consists solely of carbon dioxide, which fits with the requirements of the solar biogas reforming process, wherein the biogas upgrading step is intended to produce two gas streams: one containing only CO_2, and another comprising about 93–94 mol-% CH_4. Therefore, the proposed VSA employing CaMOF as the adsorbent may satisfy the requirements of this biogas reforming process. From an operational viewpoint, it is apparent that for a given bed mass, the vacuum pressure should be kept within a band of approximately 4 kPa from the setpoint. In terms of bed degradation such that the effective mass of accessibly adsorbent decreases, Figure 12 shows that the VSA process is less sensitive than it is to operating pressure fluctuations, as evidenced by the broader range of bed mass values for which the target concentration of 93–94 mol-% methane can be achieved. It can be noted that test calculations were performed for operations approaching 1000 kPa; however, the magnitude of methane uptake into CaMOF meant that achieving both outlet composition specifications—i.e., one gas stream with 100 mol-% CO_2 and another with 93–94 mol-% CH_4—would be challenging in practice when employing a single-stage pressure swing adsorption system.

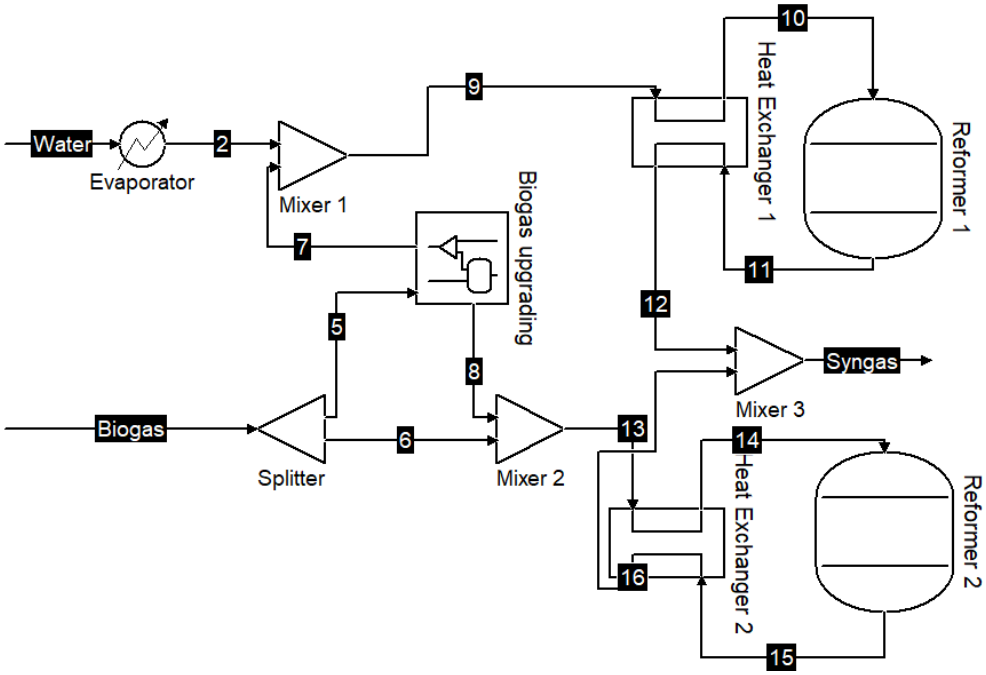

Figure 11. Flow sheet of a solar-driven biogas reforming process [96].

If one considers the correction factors mentioned in Section 3.1 to adjust the quantity of CO_2 and CH_4 adsorbed, then the batch equilibrium modelling yields a qualitatively similar result, as shown in Figure 13. Here, it is apparent that a smaller bed size over a similar operating range yields performance such that the targeted methane content of 93–94 mol-% is achievable. The required bed size in this case is about 5–6 g/mole of feedstock. Therefore, when considering this correction factor to account for consistent deviations between the available experimental data and the predictions of the COMPASS forcefield, it is apparent that CaMOF can serve as a suitable adsorbent for the solar biogas reforming process.

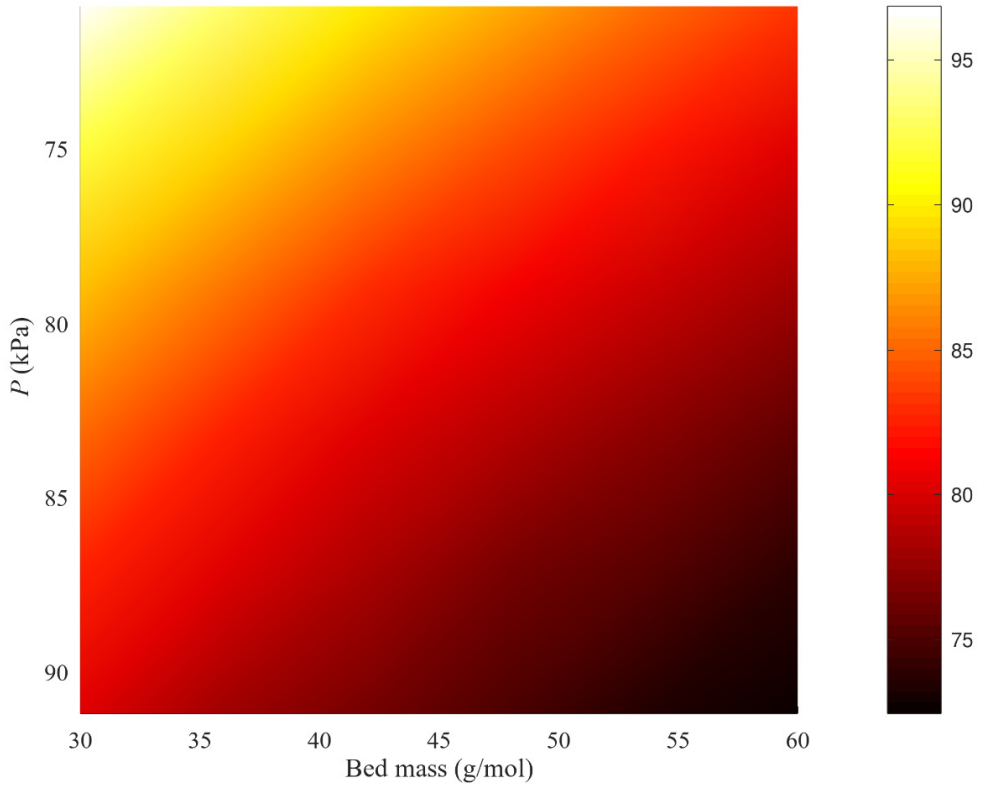

Figure 12. Heat map of CO_2 composition (in mol-%) in the outlet stream from the VSA system as a function of bed mass and operating pressure ratio.

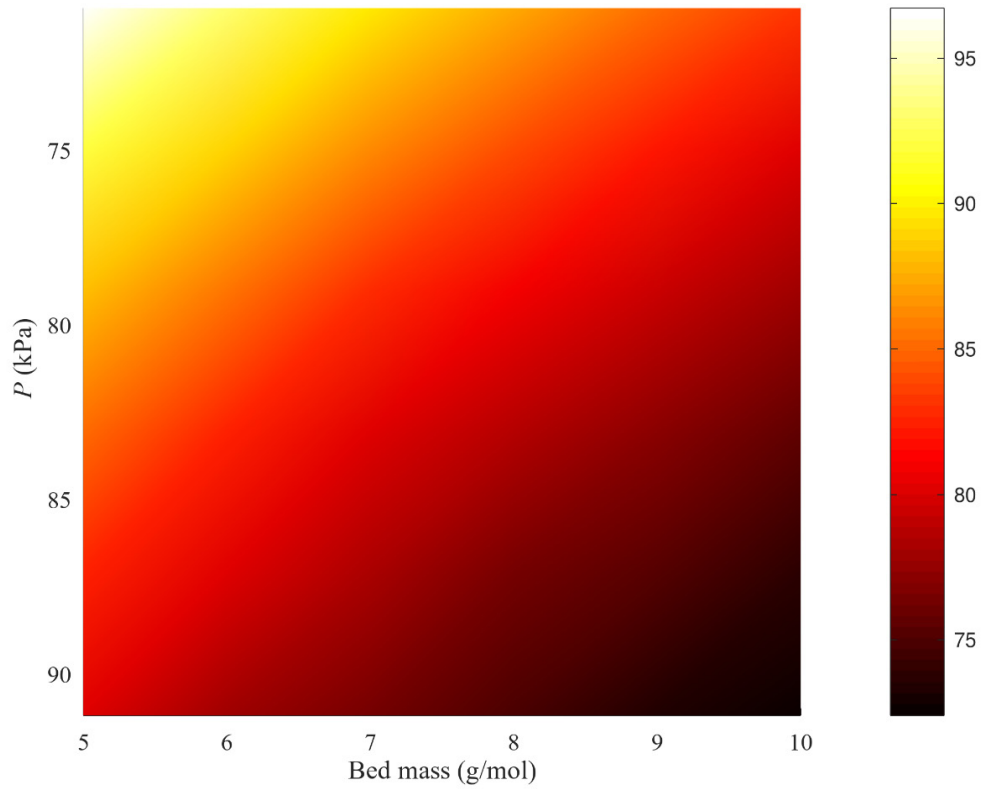

Figure 13. Heat map of CO_2 composition (in mol-%) in the outlet stream from the VSA system as a function of bed mass and operating pressure ratio, when a correction factor is incorporated to account for deviations between experiments and COMPASS forcefield predictions. Details are provided in the text in Section 3.1.

Regarding the outlook, this study integrated atomistic simulation with macro-scale batch equilibrium modelling with a view to integrating a gas separation unit with an existing chemical process design. This workflow can be employed in future work to screen multiple adsorbent materials to determine their suitability for integration into existing processes. In principle, new adsorbents can be designed in silico and then their potential for industrial application can be assessed immediately. The results obtained by such multiscale modelling are largely limited by the assumptions that go into interparticle potential energy modelling at the atomistic scale, although, in many cases, the fundamental behaviour of physisorption processes is well described by modern forcefields, and such computation screening can suggest pathways for future gas separation research. An advantage of this multiscale modelling approach is that highly variable feedstocks can be considered, which is a feature of biomass-derived products. Hence, this modelling approach can assist in rapidly adjusting existing processes or designing new ones to take advantage of the features of novel or inconsistent biogas or biomass-derived feedstocks.

5. Conclusions

Atomistic Monte Carlo simulations in the grand canonical ensemble were employed to study the sorption of biogas constituents on CaMOF to assess, in silico, its potential usefulness to purify biogas via sorption processes such as pressure or vacuum swing adsorption. The hydrogen sulphide displayed unusual behaviour in that it had two or three different adsorption site types within the CaMOF (based on an assessment of the potential energy of the simulation cell), complicating any description of hydrogen sulphide adsorption on CaMOF in terms of common adsorption isotherm models. With respect to the other species under consideration (i.e., nitrogen, oxygen, methane, hydrogen, and carbon dioxide), commonly used adsorption isotherm models adequately described the observed sorption behaviour.

Simulations of mixture adsorption were also undertaken, for which it was observed that the optimal removal of non-calorific components occurred at vacuum pressure (specifically at 10 kPa, the lowest pressure considered in this study). The strong selectivity of the CaMOF adsorbent in favour of hydrogen sulphide at low pressures suggests that future experimental work may yield a practicable vacuum swing adsorption system to produce cleaner-burning biogas free from sulphurous impurities and with reduced non-calorific content. In addition, low-sulphur biogas cleaned using vacuum swing adsorption in this way may be beneficial to steam reforming operations using renewable biogas feedstocks.

In addition to molecular simulations, batch equilibrium modelling was undertaken with a view to assessing the feasibility of the CaMOF as an adsorbent for the vacuum swing adsorption separation of a CH_4/CO_2 mixture. This was undertaken within the context of solar biogas reforming, where the effects of operating pressure and bed size for a single-bed adsorber were examined. It was demonstrated that this unit may be incorporated into a solar biogas reforming process, as it can meet the requirements of the biogas feed preparation step in terms of separation power. A downside to consider, however, is that there may be challenges with adsorbent regenerability to be overcome, as indicated by an assessment of the isosteric heat of adsorption of H_2S.

Supplementary Materials: The following supporting information can be downloaded at: https://www.mdpi.com/article/10.3390/chemengineering8030062/s1, Figure S1: Effect of simulation cell size on adsorption of carbon dioxide in CaMOF at 298 K; Figure S2: Effect of van der Waals cut-off radius on adsorption of carbon dioxide in CaMOF at 298 K.

Author Contributions: Conceptualisation, M.L. and K.T.; methodology, M.L. and V.T.A.; software, M.L.; validation, M.L. and K.T.; formal analysis, M.L., V.T.A. and K.T.; investigation, M.L. and V.T.A.; resources, M.L.; data curation, M.L.; writing—original draft preparation, M.L.; writing—review and editing, M.L., V.T.A. and K.T.; visualisation, M.L.; supervision, M.L. and K.T.; project administration, M.L. All authors have read and agreed to the published version of the manuscript.

Funding: This research received no external funding.

Data Availability Statement: The raw data supporting the conclusions of this article will be made available by the authors on request.

Acknowledgments: All simulations were performed using the facilities of the Centre for High Performance Computing (CHPC) in Cape Town, South Africa. This work is supported by the National Research Foundation (NRF) through its Rated Researcher programme, and by the Department of Higher Education and Training (DHET) through its Future Professors Programme (FPP).

Conflicts of Interest: The authors declare no conflicts of interest.

References

1. Yoon, S.H.; Lee, C.S. Experimental investigation on the combustion and exhaust emission characteristics of biogas–biodiesel dual-fuel combustion in a CI engine. *Fuel Process. Technol.* **2011**, *92*, 992–1000. [CrossRef]
2. Ribeiro, N.d.S.; Barros, R.M.; dos Santos, I.F.S.; Filho, G.L.T.; da Silva, S.P.G. Electric energy generation from biogas derived from municipal solid waste using two systems: Landfills and anaerobic digesters in the states of São Paulo and Minas Gerais, Brazil. *Sustain. Energy Technol. Assess.* **2021**, *48*, 101552. [CrossRef]
3. Legrottaglie, F.; Mattarelli, E.; Rinaldini, C.A.; Scrignoli, F. Application to micro-cogeneration of an innovative dual fuel compression ignition engine running on biogas. *Int. J. Thermofluids* **2021**, *10*, 100093. [CrossRef]
4. Papurello, D.; Silvestri, S.; Biasioli, F.; Lombardi, L. Wood ash biomethane upgrading system: A case study. *Renew. Energy* **2021**, *182*, 702–712. [CrossRef]
5. Caetano, B.C.; Santos, N.D.S.A.; Hanriot, V.M.; Sandoval, O.R.; Huebner, R. Energy conversion of biogas from livestock manure to electricity energy using a Stirling engine. *Energy Convers. Manag. X* **2022**, *15*, 100224. [CrossRef]
6. Hammer, G.; Lübcke, T.; Kettner, R.; Pillarella, M.R.; Recknagel, H.; Commichau, A.; Neumann, H.-J.; Paczynska-Lahme, B. Natural Gas. In *Ullmann's Encyclopedia of Industrial Chemistry*; Wiley: Hoboken, NJ, USA, 2006. [CrossRef]
7. Kapoor, R.; Ghosh, P.; Kumar, M.; Vijay, V.K. Evaluation of biogas upgrading technologies and future perspectives: A review. *Environ. Sci. Pollut. Res.* **2019**, *26*, 11631–11661. [CrossRef] [PubMed]
8. Khan, M.U.; Lee, J.T.E.; Bashir, M.A.; Dissanayake, P.D.; Ok, Y.S.; Tong, Y.W.; Shariati, M.A.; Wu, S.; Ahring, B.K. Current status of biogas upgrading for direct biomethane use: A review. *Renew. Sustain. Energy Rev.* **2021**, *149*, 111343. [CrossRef]
9. Golmakani, A.; Nabavi, S.A.; Wadi, B.; Manovic, V. Advances, challenges, and perspectives of biogas cleaning, upgrading, and utilisation. *Fuel* **2022**, *317*, 123085. [CrossRef]
10. Hosseini, S.S.; Denayer, J.F.M. Biogas upgrading by adsorption processes: Mathematical modeling, simulation and optimization approach—A review. *J. Environ. Chem. Eng.* **2022**, *10*, 107483. [CrossRef]
11. Bhoyate, S.; Kahol, P.K.; Gupta, R.K. Nanostructured materials for supercapacitor applications. In *Nanoscience*; Thomas, P.J., Revaprasadu, N., Eds.; The Royal Society of Chemistry: London, UK, 2018; Volume 5, pp. 1–29. [CrossRef]
12. Choi, J.; Ingsel, T.; Neupane, D.; Mishra, S.R.; Kumar, A.; Gupta, R.K. Metal-organic framework-derived cobalt oxide and sulfide having nanoflowers architecture for efficient energy conversion and storage. *J. Energy Storage* **2022**, *50*, 104145. [CrossRef]
13. Li, J.-R.; Sculley, J.; Zhou, H.-C. Metal–Organic Frameworks for Separations. *Chem. Rev.* **2012**, *112*, 869–932. [CrossRef]
14. Lawson, H.D.; Walton, S.P.; Chan, C. Metal–Organic Frameworks for Drug Delivery: A Design Perspective. *ACS Appl. Mater. Interfaces* **2021**, *13*, 7004–7020. [CrossRef] [PubMed]
15. Ma, X.; Kang, J.; Wu, Y.; Pang, C.; Li, S.; Li, J.; Xiong, Y.; Luo, J.; Wang, M.; Xu, Z. Recent advances in metal/covalent organic framework-based materials for photoelectrochemical sensing applications. *TrAC Trends Anal. Chem.* **2022**, *157*, 116793. [CrossRef]
16. Mageto, T.; de Souza, F.M.; Kaur, J.; Kumar, A.; Gupta, R.K. Chemistry and potential candidature of metal-organic frameworks for electrochemical energy storage devices. *Fuel Process. Technol.* **2023**, *242*, 107659. [CrossRef]
17. Jiao, L.; Jiang, H.-L. Metal-organic frameworks for catalysis: Fundamentals and future prospects. *Chin. J. Catal.* **2023**, *45*, 1–5. [CrossRef]
18. Gulati, S.; Vijayan, S.; Mansi; Kumar, S.; Harikumar, B.; Trivedi, M.; Varma, R.S. Recent advances in the application of metal-organic frameworks (MOFs)-based nanocatalysts for direct conversion of carbon dioxide (CO_2) to value-added chemicals. *Coord. Chem. Rev.* **2023**, *474*, 214853. [CrossRef]
19. Russo, V.; Hmoudah, M.; Broccoli, F.; Iesce, M.R.; Jung, O.-S.; Di Serio, M. Applications of Metal Organic Frameworks in Wastewater Treatment: A Review on Adsorption and Photodegradation. *Front. Chem. Eng.* **2020**, *2*, 581487. Available online: https://www.frontiersin.org/articles/10.3389/fceng.2020.581487 (accessed on 24 April 2024). [CrossRef]
20. Hou, Y.; Liu, M.; Zhang, L.; Li, M.; Wang, D.; Liu, J.; Fu, S. Matchstick-like metal-organic framework-based superwetting materials for efficient multiphase liquid separation via filtration or adsorption. *Sep. Purif. Technol.* **2020**, *240*, 116598. [CrossRef]
21. Taddei, M.; Petit, C. Engineering metal–organic frameworks for adsorption-based gas separations: From process to atomic scale. *Mol. Syst. Des. Eng.* **2021**, *6*, 841–875. [CrossRef]
22. Wang, X.-J.; Li, P.-Z.; Liu, L.; Zhang, Q.; Borah, P.; Wong, J.D.; Chan, X.X.; Rakesh, G.; Li, Y.; Zhao, Y. Significant gas uptake enhancement by post-exchange of zinc(ii) with copper(ii) within a metal–organic framework. *Chem. Commun.* **2012**, *48*, 10286–10288. [CrossRef]
23. Avci, G.; Erucar, I.; Keskin, S. Do New MOFs Perform Better for CO_2 Capture and H_2 Purification? Computational Screening of the Updated MOF Database. *ACS Appl. Mater. Interfaces* **2020**, *12*, 41567–41579. [CrossRef] [PubMed]

24. Bao, Z.; Wang, J.; Zhang, Z.; Xing, H.; Yang, Q.; Yang, Y.; Wu, H.; Krishna, R.; Zhou, W.; Chen, B.; et al. Molecular sieving of ethane from ethylene through the molecular cross-section size differentiation in gallate-based metal–organic frameworks. *Angew. Chem.* **2018**, *130*, 16252–16257. [CrossRef]
25. Du, M.; Li, C.-P.; Chen, M.; Ge, Z.-W.; Wang, X.; Wang, L.; Liu, C.-S. Divergent Kinetic and Thermodynamic Hydration of a Porous Cu(II) Coordination Polymer with Exclusive CO2 Sorption Selectivity. *J. Am. Chem. Soc.* **2014**, *136*, 10906–10909. [CrossRef] [PubMed]
26. Assen, A.H.; Belmabkhout, Y.; Adil, K.; Bhatt, P.M.; Xue, D.-X.; Jiang, H.; Eddaoudi, M. Ultra-tuning of the rare-earth fcu-MOF aperture size for selective molecular exclusion of branched paraffins. *Angew. Chem. Int. Ed.* **2015**, *54*, 14353–14358. [CrossRef] [PubMed]
27. Lin, R.-B.; Xiang, S.; Zhou, W.; Chen, B. Microporous metal-organic framework materials for gas separation. *Chem* **2020**, *6*, 337–363. [CrossRef]
28. Vivo-Vilches, J.F.; Pérez-Cadenas, A.F.; Maldonado-Hódar, F.J.; Carrasco-Marín, F.; Faria, R.P.; Ribeiro, A.M.; Ferreira, A.F.; Rodrigues, A.E. Biogas upgrading by selective adsorption onto CO2 activated carbon from wood pellets. *J. Environ. Chem. Eng.* **2017**, *5*, 1386–1393. [CrossRef]
29. Chaemchuen, S.; Kabir, N.A.; Zhou, K.; Verpoort, F. Metal–organic frameworks for upgrading biogas via CO2 adsorption to biogas green energy. *Chem. Soc. Rev.* **2013**, *42*, 9304–9332. [CrossRef] [PubMed]
30. Wang, G.-D.; Li, Y.-Z.; Zhang, W.-F.; Hou, L.; Wang, Y.-Y.; Zhu, Z. Acetylene Separation by a Ca-MOF Containing Accessible Sites of Open Metal Centers and Organic Groups. *ACS Appl. Mater Interfaces* **2021**, *13*, 58862–58870. [CrossRef] [PubMed]
31. Chen, L.; Morrison, C.A.; Düren, T. Improving Predictions of Gas Adsorption in Metal–Organic Frameworks with Coordinatively Unsaturated Metal Sites: Model Potentials, ab initio Parameterization, and GCMC Simulations. *J. Phys. Chem. C* **2012**, *116*, 18899–18909. [CrossRef]
32. Wong-Foy, A.G.; Matzger, A.J.; Yaghi, O.M. Exceptional H2 Saturation Uptake in Microporous Metal−Organic Frameworks. *J. Am. Chem. Soc.* **2006**, *128*, 3494–3495. [CrossRef]
33. Zhou, W.; Wu, H.; Yildirim, T. Enhanced H_2 Adsorption in Isostructural Metal−Organic Frameworks with Open Metal Sites: Strong Dependence of the Binding Strength on Metal Ions. *J. Am. Chem. Soc.* **2008**, *130*, 15268–15269. [CrossRef] [PubMed]
34. Yazaydın, A.; Snurr, R.Q.; Park, T.-H.; Koh, K.; Liu, J.; LeVan, M.D.; Benin, A.I.; Jakubczak, P.; Lanuza, M.; Galloway, D.B.; et al. Screening of Metal−Organic Frameworks for Carbon Dioxide Capture from Flue Gas Using a Combined Experimental and Modeling Approach. *J. Am. Chem. Soc.* **2009**, *131*, 18198–18199. [CrossRef] [PubMed]
35. Chowdhury, P.; Bikkina, C.; Meister, D.; Dreisbach, F.; Gumma, S. Comparison of adsorption isotherms on Cu-BTC metal organic frameworks synthesized from different routes. *Microporous Mesoporous Mater.* **2009**, *117*, 406–413. [CrossRef]
36. Wuttke, S.; Bazin, P.; Vimont, A.; Serre, C.; Seo, Y.; Hwang, Y.K.; Chang, J.; Férey, G.; Daturi, M. Discovering the Active Sites for C_3 Separation in MIL-100(Fe) by Using Operando IR Spectroscopy. *Chem.—A Eur. J.* **2012**, *18*, 11959–11967. [CrossRef] [PubMed]
37. Britt, D.; Furukawa, H.; Wang, B.; Glover, T.G.; Yaghi, O.M. Highly efficient separation of carbon dioxide by a metal-organic framework replete with open metal sites. *Proc. Natl. Acad. Sci. USA* **2009**, *106*, 20637–20640. [CrossRef] [PubMed]
38. Wang, Q.M.; Shen, D.; Bülow, M.; Lau, M.L.; Deng, S.; Fitch, F.R.; Lemcoff, N.O.; Semanscin, J. Metallo-organic molecular sieve for gas separation and purification. *Microporous Mesoporous Mater.* **2002**, *55*, 217–230. [CrossRef]
39. Bae, Y.-S.; Farha, O.K.; Spokoyny, A.M.; Mirkin, C.A.; Hupp, J.T.; Snurr, R.Q. Carborane-based metal–organic frameworks as highly selective sorbents for CO_2 over methane. *Chem. Commun.* **2008**, *35*, 4135–4137. [CrossRef] [PubMed]
40. Xamena, F.X.L.I.; Corma, A.; Garcia, H. Applications for Metal−Organic Frameworks (MOFs) as Quantum Dot Semiconductors. *J. Phys. Chem. C* **2007**, *111*, 80–85. [CrossRef]
41. Vitillo, J.G.; Regli, L.; Chavan, S.; Ricchiardi, G.; Spoto, G.; Dietzel, P.D.C.; Bordiga, S.; Zecchina, A. Role of Exposed Metal Sites in Hydrogen Storage in MOFs. *J. Am. Chem. Soc.* **2008**, *130*, 8386–8396. [CrossRef]
42. Canivet, J.; Vandichel, M.; Farrusseng, D. Origin of highly active metal–organic framework catalysts: Defects? Defects! *Dalton Trans.* **2016**, *45*, 4090–4099. [CrossRef]
43. Kim, H.K.; Yun, W.S.; Kim, M.-B.; Kim, J.Y.; Bae, Y.-S.; Lee, J.; Jeong, N.C. A Chemical Route to Activation of Open Metal Sites in the Copper-Based Metal–Organic Framework Materials HKUST-1 and Cu-MOF-2. *J. Am. Chem. Soc.* **2015**, *137*, 10009–10015. [CrossRef] [PubMed]
44. Mitchell, L.; Gonzalez-Santiago, B.; Mowat, J.P.S.; Gunn, M.E.; Williamson, P.; Acerbi, N.; Clarke, M.L.; Wright, P.A. Remarkable Lewis acid catalytic performance of the scandium trimesate metal organic framework MIL-100(Sc) for C–C and C=N bond-forming reactions. *Catal. Sci. Technol.* **2013**, *3*, 606–617. [CrossRef]
45. Chui, S.S.-Y.; Lo, S.M.-F.; Charmant, J.P.H.; Orpen, A.G.; Williams, I.D. A Chemically Functionalizable Nanoporous Material $[Cu_3(TMA)_2(H_2O)_3]$n. *Science* **1999**, *283*, 1148–1150. [CrossRef] [PubMed]
46. Yoon, J.W.; Seo, Y.; Hwang, Y.K.; Chang, J.; Leclerc, H.; Wuttke, S.; Bazin, P.; Vimont, A.; Daturi, M.; Bloch, E.; et al. Controlled Reducibility of a Metal–Organic Framework with Coordinatively Unsaturated Sites for Preferential Gas Sorption. *Angew. Chem. Int. Ed.* **2010**, *49*, 5949–5952. [CrossRef] [PubMed]
47. Férey, G.; Serre, C.; Mellot-Draznieks, C.; Millange, F.; Surblé, S.; Dutour, J.; Margiolaki, I. A hybrid solid with giant pores prepared by a combination of targeted chemistry, simulation, and powder diffraction. *Angew. Chem.* **2004**, *116*, 6456–6461. [CrossRef]

48. Cavka, J.H.; Jakobsen, S.; Olsbye, U.; Guillou, N.; Lamberti, C.; Bordiga, S.; Lillerud, K.P. A New Zirconium Inorganic Building Brick Forming Metal Organic Frameworks with Exceptional Stability. *J. Am. Chem. Soc.* **2008**, *130*, 13850–13851. [CrossRef]
49. Dietzel, P.D.C.; Panella, B.; Hirscher, M.; Blom, R.; Fjellvåg, H. Hydrogen adsorption in a nickel based coordination polymer with open metal sites in the cylindrical cavities of the desolvated framework. *Chem. Commun.* **2006**, *9*, 959–961. [CrossRef]
50. Metropolis, N.; Rosenbluth, A.W.; Rosenbluth, M.N.; Teller, A.H.; Teller, E. Equation of State Calculations by Fast Computing Machines. *J. Chem. Phys.* **1953**, *21*, 1087–1092. [CrossRef]
51. Peng, D.-Y.; Robinson, D.B. A New Two-Constant Equation of State. *Ind. Eng. Chem. Fundam.* **1976**, *15*, 59–64. [CrossRef]
52. Lopez-Echeverry, J.S.; Reif-Acherman, S.; Araujo-Lopez, E. Peng-Robinson equation of state: 40 years through cubics. *Fluid Phase Equilibria* **2017**, *447*, 39–71. [CrossRef]
53. Frenkel, D.; Smit, B. *Understanding Molecular Simulation: From Algorithms to Applications*; Elsevier: Amsterdam, The Netherlands, 2023.
54. BIOVIA, Dassault Systèmes, Materials Studio 2020, Biovia, San Diego: Dassault Systèmes. | Mendeley. 2019. Available online: https://www.caecis.com/wp-content/uploads/2020/05/BIOVIA_MaterialsStudio_2019_SystemRequirements.pdf (accessed on 24 April 2024).
55. Sun, H. COMPASS: An ab Initio Force-Field Optimized for Condensed-Phase ApplicationsOverview with Details on Alkane and Benzene Compounds. *J. Phys. Chem. B* **1998**, *102*, 7338–7364. [CrossRef]
56. Martin, M.G. MCCCS Towhee: A tool for Monte Carlo molecular simulation. *Mol. Simul.* **2013**, *39*, 1212–1222. [CrossRef]
57. Einstein, A. Über die von der molekularkinetischen Theorie der Wärme geforderte Bewegung von in ruhenden Flüssigkeiten suspendierten Teilchen. *Ann. Phys.* **1905**, *4*, 549–560. [CrossRef]
58. Warshel, A.; Lifson, S. Consistent Force Field Calculations. II. Crystal Structures, Sublimation Energies, Molecular and Lattice Vibrations, Molecular Conformations, and Enthalpies of Alkanes. *J. Chem. Phys.* **1970**, *53*, 582–594. [CrossRef]
59. Waldman, M.; Hagler, A.T. New combining rules for rare gas van der waals parameters. *J. Comput. Chem.* **1993**, *14*, 1077–1084. [CrossRef]
60. Chen, C.; Zhang, M.; Zhang, W.; Bai, J. Stable Amide-Functionalized Metal–Organic Framework with Highly Selective CO_2 Adsorption. *Inorg. Chem.* **2019**, *58*, 2729–2735. [CrossRef] [PubMed]
61. Firouzjaei, M.D.; Afkhami, F.A.; Esfahani, M.R.; Turner, C.H.; Nejati, S. Experimental and molecular dynamics study on dye removal from water by a graphene oxide-copper-metal organic framework nanocomposite. *J. Water Process Eng.* **2020**, *34*, 101180. [CrossRef]
62. Yan, F.; Wang, Q.; Wang, F.; Huang, Z. Study on energy storage properties of Metal-organic frameworks nanofluids (UIO-67/Water and UIO-67/Methanol) by an experimental and theoretical method. *J. Mater. Sci.* **2021**, *56*, 10008–10017. [CrossRef]
63. Han, X.; Sun, H.; Liu, L.; Wang, Y.; He, G.; Li, J. Improved desulfurization performance of polydimethylsiloxane membrane by incorporating metal organic framework CPO-27-Ni. *Sep. Purif. Technol.* **2019**, *217*, 86–94. [CrossRef]
64. Liu, P.; Wang, Y.; Chen, Y.; Yang, J.; Wang, X.; Li, L.; Li, J. Construction of saturated coordination titanium-based metal–organic framework for one-step C2H2/C2H6/C2H4 separation. *Sep. Purif. Technol.* **2021**, *276*, 119284. [CrossRef]
65. Chen, J.-J.; Li, W.-W.; Li, X.-L.; Yu, H.-Q. Improving Biogas Separation and Methane Storage with Multilayer Graphene Nanostructure via Layer Spacing Optimization and Lithium Doping: A Molecular Simulation Investigation. *Environ. Sci. Technol.* **2012**, *46*, 10341–10348. [CrossRef]
66. Lasich, M. Sorption of natural gas in cement hydrate by Monte Carlo simulation. *Eur. Phys. J. B* **2018**, *91*, 299. [CrossRef]
67. Moradi, M.; Azizpour, H.; Yavari, M.; Khoshnevisan, N. Estimation of Diffusion Coefficient of Benzene/Hexane Mixtures by Molecular Dynamics Simulation. *J. Chem. Pet. Eng.* **2023**, *52*, 199–207.
68. Chen, G.; An, Y.; Shen, Y.; Wang, Y.; Tang, Z.; Lu, B.; Zhang, D. Effect of pore size on CH_4/N_2 separation using activated carbon. *Chin. J. Chem. Eng.* **2020**, *28*, 1062–1068. [CrossRef]
69. Allen, M.P.; Tildesley, D.J. Computer simulation of liquids. *Clarendon-0.12* **1987**.
70. Papadimitriou, N.I.; Tsimpanogiannis, I.N.; Papaioannou, A.T.; Stubos, A.K. Evaluation of the Hydrogen-Storage Capacity of Pure H2 and Binary H2-THF Hydrates with Monte Carlo Simulations. *J. Phys. Chem. C* **2008**, *112*, 10294–10302. [CrossRef]
71. Lasich, M.; Narasigadu, C.; Moodley, S. Adsorption of humid air in compacted montmorillonite: A Monte Carlo simulation study. *Fluid Phase Equilibria* **2019**, *487*, 52–57. [CrossRef]
72. Zhao, Y.; Seredych, M.; Jagiello, J.; Zhong, Q.; Bandosz, T.J. Insight into the mechanism of CO2 adsorption on Cu–BTC and its composites with graphite oxide or aminated graphite oxide. *Chem. Eng. J.* **2014**, *239*, 399–407. [CrossRef]
73. Chanajaree, R.; Sailuam, W.; Seehamart, K. Molecular self-diffusivity and separation of CH_4/H_2S in metal organic framework MIL-47(V). *Microporous Mesoporous Mater.* **2022**, *335*, 111783. [CrossRef]
74. Nosé, S. A unified formulation of the constant temperature molecular dynamics methods. *J. Chem. Phys.* **1984**, *81*, 511–519. [CrossRef]
75. Hoover, W.G. Canonical dynamics: Equilibrium phase-space distributions. *Phys. Rev. A* **1985**, *31*, 1695–1697. [CrossRef] [PubMed]
76. Verlet, L. Computer 'Experiments' on Classical Fluids. I. Thermodynamical Properties of Lennard-Jones Molecules. *Phys. Rev.* **1967**, *159*, 98–103. [CrossRef]
77. Ewald, P.P. Die Berechnung optischer und elektrostatischer Gitterpotentiale. *Ann. Phys.* **1921**, *369*, 253–287. [CrossRef]
78. Langmuir, I. The constitution and fundamental properties of solids and liquids. Part I. Solids. *J. Am. Chem. Soc.* **1916**, *38*, 2221–2295. [CrossRef]

79. Freundlich, H.M.F. Over the adsorption in solution. *J. Phys. Chem.* **1906**, *57*, 1100–1107.
80. Temkin, M.I. Kinetics of ammonia synthesis on promoted iron catalysts. *Acta Physicochim. URSS* **1940**, *12*, 327–356.
81. Redlich, O.; Peterson, D.L. A Useful Adsorption Isotherm. *J. Phys. Chem.* **1959**, *63*, 1024. [CrossRef]
82. Sips, R. On the Structure of a Catalyst Surface. *J. Chem. Phys.* **1948**, *16*, 490–495. [CrossRef]
83. Eaton, J.W.; Bateman, D.; Hauberg, S. *GNU Octave Version 3.0. 1 Manual: A High-Level Interactive Language for Numerical Computations*; SoHo Books: New York, NY, USA, 2007.
84. Chung, Y.; Na, B.-K.; Song, H.K. Short-cut evaluation of pressure swing adsorption systems. *Comput. Chem. Eng.* **1998**, *22*, S637–S640. [CrossRef]
85. Lasich, M. Upgrading Wood Gas Using Bentonite Clay: A Multiscale Modeling and Simulation Study. *ACS Omega* **2020**, *5*, 11068–11074. [CrossRef]
86. Akaike, H. A new look at the statistical model identification. *IEEE Trans. Autom. Contr.* **1974**, *19*, 716–723. [CrossRef]
87. Cavanaugh, J.E. Unifying the derivations for the Akaike and corrected Akaike information criteria. *Stat. Probab. Lett.* **1997**, *33*, 201–208. [CrossRef]
88. Vivo-Vilches, J.F.; Pérez-Cadenas, A.F.; Maldonado-Hódar, F.J.; Carrasco-Marín, F.; Regufe, M.J.; Ribeiro, A.M.; Ferreira, A.F.P.; Rodrigues, A.E. Resorcinol–formaldehyde carbon xerogel as selective adsorbent of carbon dioxide present on biogas. *Adsorption* **2018**, *24*, 169–177. [CrossRef]
89. Liu, G.; Cadiau, A.; Liu, Y.; Adil, K.; Chernikova, V.; Carja, I.-D.; Belmabkhout, Y.; Karunakaran, M.; Shekhah, O.; Zhang, C.; et al. Enabling fluorinated MOF-based membranes for simultaneous removal of H_2S and CO_2 from natural gas. *Angew. Chem.* **2018**, *130*, 15027–15032. [CrossRef]
90. Cavenati, S.; Grande, C.A.; Rodrigues, A.E.; Kiener, C.; Müller, U. Metal Organic Framework Adsorbent for Biogas Upgrading. *Ind. Eng. Chem. Res.* **2008**, *47*, 6333–6335. [CrossRef]
91. Himeno, S.; Komatsu, T.; Fujita, S. High-Pressure Adsorption Equilibria of Methane and Carbon Dioxide on Several Activated Carbons. *J. Chem. Eng. Data* **2005**, *50*, 369–376. [CrossRef]
92. Ghanbari, R.; Marandi, A.; Zare, E.N. Development of melamine-based covalent organic framework-MOF pearl-like heterostructure integrated poly(ether-block-amide) for CO_2/CH_4 separation. *J. Environ. Chem. Eng.* **2023**, *11*, 109269. [CrossRef]
93. Chen, Z.; Xiang, S.; Arman, H.D.; Li, P.; Zhao, D.; Chen, B. Significantly Enhanced CO2/CH4 Separation Selectivity within a 3D Prototype Metal–Organic Framework Functionalized with OH Groups on Pore Surfaces at Room Temperature. *Eur. J. Inorg. Chem.* **2011**, *2011*, 2227–2231. [CrossRef]
94. Hamon, L.; Jolimaître, E.; Pirngruber, G.D. CO_2 and CH_4 Separation by Adsorption Using Cu-BTC Metal−Organic Framework. *Ind. Eng. Chem. Res.* **2010**, *49*, 7497–7503. [CrossRef]
95. Luyben, W.L. Optimum vacuum distillation pressure. *Chem. Eng. Process.—Process Intensif.* **2022**, *171*, 108630. [CrossRef]
96. Su, B.; Han, W.; He, H.; Jin, H.; Chen, Z.; Zheng, J.; Yang, S.; Zhang, X. Using moderate carbon dioxide separation to improve the performance of solar-driven biogas reforming process. *Appl. Energy* **2020**, *279*, 115693. [CrossRef]